Atmospheric
Chemistry
and Physics
Discussions

Retrieval of ice nucleating particle concentrations from lidar observations: Comparison with airborne in-situ measurements from UAVs

Eleni Marinou[1,2,3], Matthias Tesche[4], Athanasios Nenes[5,6,7,8], Albert Ansmann[9], Jann Schrod[10], Dimitra Mamali[11], Alexandra Tsekeri[2], Michael Pikridas[12], Holger Baars[9], Ronny Engelmann[9], Kalliopi - Artemis Voudouri[3], Stavros Solomos[2], Jean Sciare[12], Silke Groß[1], and Vassilis Amiridis[2]

[1]Institute of Atmospheric Physics, German Aerospace Center (DLR), Oberpfaffenhofen, 82234, Germany
[2]IAASARS, National Observatory of Athens, Athens, 15236, Greece
[3]Department of Physics, Aristotle University of Thessaloniki, Thessaloniki, 54124, Greece
[4]University of Hertfordshire, College Lane, AL10 9AB Hatfield, United Kingdom
[5]Laboratory of Atmospheric processes and Their Impact (LAPI), School of Architecture, Civil and Environmental Engineering, École Polytechnique Fédérale de Lausanne, CH-1015, Switzerland
[6]School of Earth Atmospheric Sciences, Georgia Institute of Technology, Atlanta, GA, 30332, USA
[7]IERSD, National Observatory of Athens, Athens, 15236, Greece
[8]Institute of Chemical Engineering Sciences, Foundation for Research and Technology, Hellas, Patras, 26504, Greece
[9]Leibniz Institute for Tropospheric Research, 04318 Leipzig, Germany
[10]Institute for Atmospheric and Environmental Sciences, Goethe University Frankfurt, 60438, Frankfurt am Main, Germany
[11]Department of Geoscience and Remote Sensing, Delft University of Technology, Delft, The Netherlands
[12]The Cyprus Institute, Energy, Environment and Water Research Centre, Nicosia, Cyprus

Correspondence to: Eleni Marinou (elmarinou@noa.gr)

Abstract.

Aerosols that are efficient ice nucleating particles (INPs) are crucial for the formation of cloud ice via heterogeneous nucleation in the atmosphere. The distribution of INPs on a large spatial scale and as a function of height determines their impact on clouds and climate. However, in-situ measurements of INPs provide sparse coverage over space and time. A promising

5　approach to address this gap is to retrieve INP concentration profiles by combining particle concentration profiles derived by lidar measurements with INP efficiency parameterization for different freezing mechanisms (immersion freezing, deposition nucleation). Here, we assess the feasibility of this new method for both ground-based and space-borne lidar measurements, using airborne in-situ observations from an experimental campaign at Cyprus in April 2016. Analyzing five case studies we calculated the particle number concentrations using lidar measurements (with an uncertainty of 20 to 100%) and we assessed

10　the suitability of the different INP parameterizations with respect to the temperature range and the type of particles considered. Specifically, our analysis suggests that the parameterization of Ullrich et al. (2017) (applicable for the temperature range $-50\,°C$ to $-33\,°C$) agree within 1 order of magnitude with the in-situ observations of n_{INP} and can efficiently address the deposition nucleation pathway in dust-dominated environments. Additionally, the combination of the parameterizations of DeMott et al. (2015) and DeMott et al. (2010) (applicable for the temperature range $-35\,°C$ to $-9\,°C$) agree within 2 or-

15　ders of magnitude with the in-situ observations of n_{INP} and can efficiently address the immersion/condensation pathway of

dust and continental/anthropogenic particles. The same conclusion is derived from the compilation of the parameterizations of DeMott et al. (2015) for dust and Ullrich et al. (2017) for soot. Furthermore, we applied this methodology to estimate the INP concentration profiles before and after a cloud formation, indicating the seeding role of the particles and their subsequent impact on cloud formation and characteristics. More synergistic data-sets are expected to become available in the future from

5 EARLINET (European Aerosol Research Lidar NETwork) and in the frame of the European ACTRIS-RI (Aerosols, Clouds, and Trace gases Research Infrastructure). Our analysis shown that the developed techniques, when applied on CALIPSO (Cloud-Aerosol Lidar and Infrared Pathfinder Satellite Observations) space-born lidar observations, are in very good agreement with the in-situ measurements. This study give us confidence for the production of global 3D products of $n_{250,\text{dry}}$, S_{dry} and n_{INP} using the CALIPSO 13-yrs dataset. This could provide valuable insight into global height-resolved distribution of

10 INP concentrations related to mineral dust, and possibly other aerosol types.

1 Introduction

The interaction of aerosol particles with clouds, and the related climatic effects have been in the focus of atmospheric research for several decades. Aerosols can act as cloud condensation nuclei (CCN) in liquid water clouds and as ice nucleating particles (INPs) in mixed-phase and ice clouds. Changes in their concentration affect cloud extent, lifetime, particle size and radiative

15 properties (Lohmann and Feichter, 2005; Tao et al., 2012; Altaratz et al., 2014; Rosenfeld et al., 2014). As important these interactions are, they are the source of the most uncertainty in assessing anthropogenic climate change (IPCC Fifth Assessment Report, Seinfeld et al. 2016).

All clouds producing ice require, for temperatures above $\sim -35\,^\circ$C, the presence of INPs. Compared to CCN, INPs are rare (about 1 in a million aerosol particles act as INP), and become increasingly sparse with increasing temperature (Pruppacher and Klett,

20 1997). Aerosol species which have been identified in the past as potentially important INPs are mineral dust, biological species (pollen, bacteria, fungal spores and plankton), carbonaceous combustion products, soot, volcanic ash and sea spray (Murray et al., 2012; DeMott et al., 2015b). From these aerosol types, mineral dust and soot are efficient INPs at temperatures below $-15\,^\circ$C to $-20\,^\circ$C (dust) and $-40\,^\circ$C (soot) and they have been studied extensively for their INP properties in field experiments and laboratory studies (Twohy et al., 2009, 2017; Kamphus et al., 2010; Hoose and Möhler, 2012; Murray et al.,

25 2012; Sullivan et al., 2016; Ullrich et al., 2017). Biological particles are one of the most active INP species, however their abundance is likely low on a global scale, particularly compared to other sources such as mineral dusts (Morris et al., 2014). It has been suggested that soil and clay particles may act as carriers of biological nanoscale INPs (e.g. proteins), which could potentially contribute to a globally/locally relevant source of INP (Schnell and Vali, 1976; O'Sullivan et al., 2014, 2015, 2016). Moreover, marine aerosols (with possible influence of a biological microlayer close to the surface) are also important INPs

30 in areas where mineral dust influence is less pronounced (e.g. Southern Ocean; Wilson et al. (2015); Vergara-Temprado et al. (2017)).

There is a variety of pathways for heterogeneous ice nucleation: contact freezing, immersion freezing, condensation freezing and deposition nucleation (Vali et al., 2015). Individual ice nucleation pathways dominate at a characteristic temperature and

Atmospheric
Chemistry
and Physics
Discussions

supersaturation range. Field observation studies have shown that immersion freezing dominates at temperatures higher than $-30\,^{\circ}\mathrm{C}$, while deposition nucleation dominates below $-35\,^{\circ}\mathrm{C}$ (Ansmann et al., 2005; Westbrook et al., 2011; de Boer et al., 2011). The factors that regulate the efficiency of heterogeneous ice nucleation are qualitatively understood, but no general theory of heterogeneous ice nucleation exists yet. It has been shown that in regions not influenced by sea salt aerosol, INP

5 concentrations are strongly correlated with the number of aerosol particles with dry radius greater than 250 nm ($n_{250,\mathrm{dry}}$) which form the reservoir of favorable INPs (DeMott et al., 2010, 2015). However, we have limited knowledge on how the ice nuclei activity of these particles together with their spatial and vertical distributions depend on cloud nucleation conditions (i.e. temperature (T) and supersaturation over water (ss_{w}) and ice (ss_{i})). Furthermore, field measurements of INP concentrations are very localized in space and time, whilst there are large regions without any data at all (Murray et al., 2012). The lack of

10 data inhibits our quantitative understanding of aerosol-cloud interactions and requires new strategies for obtaining data-sets (Seinfeld et al., 2016; Bühl et al., 2016).

Active remote sensing with aerosol lidar and cloud radar provides valuable data for studying aerosol-cloud interaction since it enables observations with high vertical and temporal resolution over long time periods (Ansmann et al., 2005; Illingworth et al., 2007; Seifert et al., 2010; de Boer et al., 2011; Kanitz et al., 2011; Bühl et al., 2016). Lidar measurements can provide pro-

15 files of $n_{250,\mathrm{dry}}$ and dry surface area concentration (S_{dry}) related to mineral dust, continental pollution and marine aerosol, as described in Mamouri and Ansmann (2015, 2016). Their methodology uses lidar-derived optical parameters (i.e. particle backscatter coefficient, lidar ratio and particle depolarization ratio) to separate the contribution of mineral dust in the lidar profiles (Tesche et al., 2009) and subsequently applies sun-photometer based parameterizations to transform the quantitative optical information into profiles of aerosol mass, number, and surface-area concentration (Ansmann et al., 2012; Mamouri and Ansmann,

20 2015, 2016). The latter can then be used as input to INP parameterizations that have been obtained from laboratory and field measurements (e.g. DeMott et al. 2010; Niemand et al. 2012; DeMott et al. 2015; Steinke et al. 2015; Ullrich et al. 2017) to derive profiles of INP concentrations (n_{INP}).

The INP retrieval from the lidar measurements presented by Mamouri and Ansmann (2015, 2016) provides promising insight into atmospheric INP concentrations from remote-sensing observations. To date, there has been no other evaluation of the lidar-

25 derived profiles of $n_{250,\mathrm{dry}}$, S_{dry} and n_{INP} by means of independent in-situ observations apart from one dust case in Schrod et al. (2017). The study presented here compares $n_{250,\mathrm{dry}}$ and n_{INP} as inferred from space-borne and ground-based lidar observations to findings from airborne in-situ measurements using data from the joint experiment "INUIT-BACCHUS-ACTRIS" (Ice Nuclei Research Unit - Impact of Biogenic versus Anthropogenic emissions on Clouds and Climate: towards a Holistic UnderStanding - Aerosols, Clouds, and Trace gases Research Infrastructure) held on April 2016 in Cyprus (Schrod et al., 2017; Mamali et al.,

30 2018). The paper starts with a review of the different INP parameterizations for mineral dust, soot and continental aerosols in Section 2. Section 3 describes the instruments used in this study and the methodology to retrieve INP concentrations from lidar measurements. The results of the intercomparison between the lidar-derived and UAV-measured $n_{250,\mathrm{dry}}$ and n_{INP} profiles are presented and discussed in Section 4 before the paper closes with a summary in Section 5.

2   INP parameterizations

A variety of parameterizations has been proposed to obtain n_{INP} from aerosol concentration measurements. In particular, a global aerosol type-independent n_{INP} parameterization is introduced by (DeMott et al., 2010), dust-specific n_{INP} parameterizations are introduced by Niemand et al. (2012); DeMott et al. (2015); Steinke et al. (2015); Ullrich et al. (2017) and soot-specific

5   n_{INP} parameterizations are proposed by Ullrich et al. (2017). The aforementioned parameterizations address immersion freezing at or above water saturation and deposition nucleation for ice saturation ratios ranging from unity up to the homogeneous freezing threshold and water saturation. Table 1 provides an overview of the temperature ranges and the freezing mechanisms for which these parameterizations are applicable.

Regarding immersion freezing, the aerosols that are activated to droplets can contribute to ice formation. In turn, the ability

10   of a particle to be activated as a cloud droplet mainly depends on the cloud supersaturation, its diameter, the water adsorption characteristics and the composition of soluble coatings (Levin et al., 2005; Kumar et al., 2011a, b; Garimella et al., 2014; Begue et al., 2015). Kumar et al. (2011b) showed that all dry-generated dust samples with radius $> 50\,\text{nm}$ are activated to CCN at water supersaturation (ss_{w}) of 0.5% while the activation radius increases to $> 250\,\text{nm}$ when water supersaturation decreases to $ss_{\text{w}} \approx 0.1\%$. This is the minimum level of ss_{w} required to activate INP for immersion freezing.

15   For immersion freezing of dust particles, the parameterization of Ullrich et al. (2017) (U17-imm) (Table 1; Eq. 1) is based on heterogeneous ice nucleation experiments at the AIDA chamber of the Karlsruhe Institute of Technology. The desert dust ground samples in this study originate from seven different desert dust locations around the world (Saharan, Takla Makan, Canary Island, Israel). The parameterization quantifies the desert dust ice nucleation efficiency as a function of ice-nucleation-active surface-site density $n_{\text{s}}(T)$ and dust dry surface area concentration $S_{\text{d,dry}}$. If the CCN activated fraction is less than 50%,

20   Eq. (1) for U17-imm needs to be scaled to be representative for the CCN activated S_{dry} (Ullrich et al., 2017). In this work, we are applying U17-imm parameterization taking into consideration the total S_{dry}.

Additionally, the parameterization of DeMott et al. (2015) (D15) (Table 1; Eq. 2) addresses the immersion and condensation freezing activity of natural mineral dust particles based on both laboratory studies using the Colorado State University's (CSU) continuous flow diffusion chamber (CFDC) and atmospheric measurements in Saharan dust layers. D15 quantifies n_{INP} as

25   a function of temperature and the total number concentration of dust particles with dry radii larger than $250\,\text{nm}$ ($n_{250,\text{d,dry}}$). We note here that the ambient values of measured $n_{\text{INP}}(p, T)$ need to transferred in standard (std) pressure and temperature conditions ($n_{250,\text{d,dry}}(p_0, T_0, T)$) before the use of (Eq. 2).

For the deposition nucleation of dust particles, the parameterizations of Steinke et al. (2015) and Ullrich et al. (2017) (S15 and U17-dep, respectively) quantify the ice nucleation efficiency as a function of $S_{\text{d,dry}}$ and $n_{\text{s}}(T, S_{\text{ice}})$ with S_{ice} the ice satura-

30   tion ratio. Both are based on AIDA laboratory studies, but they have used different dust samples. U17-dep (Table 1; Eq. 3) is based on ground desert dust samples from Sahara, Takla Makan, Canary Island and Israel while S15 (Table 1; Eq. 4) is based on dust samples from Arizona which has been treated (washed, milled, treated with acid) and is much more ice active than desert dusts on average. Although S15 parameterization is based on dust samples which usually show an enhanced freezing efficiency, it is used in the NMME-DREAM model (Non-hydrostatic Mesoscale Model on E grid, Janjic et al. (2001); Dust

Atmospheric
Chemistry
and Physics
Discussions

REgional Atmospheric Model, Nickovic et al. (2001); Pérez et al. (2006)) for INP concentration estimations (Nickovic et al. , 2016). For this reason, it is included in this work.

For the ice activation of soot particles, Ullrich et al. (2017) introduced two parameterizations, one for immersion freezing (Table 1; Eq. 5) and a second one for deposition nucleation (Table 1; Eq. 6). Both are based on experiments at the AIDA

5   chamber with soot samples generated from four different devises and quantify the soot ice nucleation efficiency as a function of S_{dry} and $n_{\mathrm{s}}(T)$ (for immersion) and $n_{\mathrm{s}}(T, S_{\mathrm{ice}})$ (for deposition).

Finally, the global type-independent n_{INP} parameterization of (DeMott et al., 2010) (Table 1; Eq. 7), is based on field data collected during nine field campaigns (in Colorado, eastern Canada, Amazonia, Alaska, and Pacific Basin) and analyzed with the CSU CFDC instrument. As the majority of the samples used for D10 are non-desert continental aerosols, this INP param-

10   eterization has been considered to be suitable for addressing the immersion and condensation freezing activity of mixtures of anthropogenic haze, biomass burning smoke, biological particles, soil and road dust (Mamouri and Ansmann, 2016).

The $n_{250,\mathrm{dry}}$ and S_{dry} used in all the aforementioned parameterizations are calculated from the lidar extinction profiles as described in Section 3.2 and show in Figures A1 and A2 in the Apendix.

Figure 1 shows a summary of the different n_{INP} parameterizations for desert dust, continental and soot. Specifically, the plot

15   shows the fraction of the ice-activated particles ($f_{\mathrm{i}} = n_{\mathrm{INP}}/n_{50,\mathrm{dry}}$) for deposition (left) and immersion (right) modes. The particle concentrations used here, are derived assuming an extinction coefficient of $50\,\mathrm{Mm}^{-1}$ for each of the different aerosol types (dust, continental, soot). The shaded areas take into account a range of the extinction coefficient from $10\,\mathrm{Mm}^{-1}$ (lower limit) to $200\,\mathrm{Mm}^{-1}$ (upper limit). The error bars mark the cumulative error in f_{i} that results from the uncertainty in the lidar observations and their conversion to mass concentration as well as from the errors in the respective parameterizations. An overview of

20   the typical values and the uncertainties used for the error estimation in this study is provided in Table 2. The deposition nucleation estimations in the left panel of Figure 1 are provided for $ss_{\mathrm{i}} = 1.15$ (solid lines) and $ss_{\mathrm{i}} = (1.05, 1.1, 1.2, 1.3, 1.4)$ (dashed lines) to give a perspective on the range of possible values. Note here that although the immersion parameterizations were obtained using measurements at the temperature ranges of [-30, -14]°C (U17-imm, dust), [-35, -21]°C (D15, dust), [-34, -18]°C (U17-imm, soot) and [-35, -9]°C (D10, continental), they have been extrapolated herein to extend over the immersion-freezing

25   temperature range (dashed part of the lines in the immersion mode chart).

Figure 1 (left panel) shows that the dust ice-activated fractions obtained from S15 are several orders of magnitude higher than those of U17-imm (e.g. 4 orders of magnitude at -40°C and $ss_{\mathrm{i}} = 1.15\%$). Additionally, the ice-activation fraction obtained from the dust and soot parameterizations of U17-dep differ up to 2 orders of magnitude for temperatures lower than ∼-38°C, with soot estimations being higher than the dust ones (e.g. up to 1.5 orders of magnitude at -45°C). On the contrary, at

30   temperatures higher that -38°C the dust ice-activated fraction estimations are higher than the soot ones. Indicatively, at T = -30°C, U17-dep(dust) f_{i} is 4 orders of magnitude higher than the U17-dep(soot).

Figure 1 (right panel) shows that the dust ice-activated fractions obtained from D15 are one order of magnitude lower than those of U17-imm. As it has been reported from laboratory ice nucleation measurements and corresponding instrument intercomparisons, at a single temperature between two and four orders of magnitude differences are observed as a result of the nat-

35   ural variability of the INP active fraction (DeMott et al., 2010, 2017) or the use of different INP counters (Burkert-Kohn et al.,

Atmospheric
Chemistry
and Physics
Discussions

2017). Hereon, we consider D15 and U17-imm as the lower and upper bounds of the immersed n_{INP} estimations for dust INP populations. Figure 1 also illustrates the increase in dust f_i of up to six orders of magnitude within the mixed-phase temperature regime from $-15\,°C$ to $-35\,°C$. For a $5\,°C$ decrease, $n_{d,INP}$ increases by about one order of magnitude. Moreover, we see that

5 for T < -18°C the ice-activated fraction derived with D15 (for dessert dust) is higher than the ice-activated fraction derived with D10 (for continental) while this changes for T > -18°C. On the contrary, U17-imm of soot gives always lower f_i than the dust parameterizations. The ice-activated fractions of D10 and U17-imm (soot), at T < -18°C, have a relative difference that is always less than 60% with U17-imm (soot) being up to 2.5 times higher than D10 at -36°C and down to 2.5 times lower at -18°C. At higher temperatures they diverge with D10 exceeding U17-imm (soot) f_i by one order of magnitude at T > -11°C.

Figure 1 can, additionally, provide an indication of the error introduced in the lidar estimated n_{INP} due to errors in the
10 selected values of T and ss_i. As we see in the right panel, for immersion mode, a $5°$ error in the assumed T can introduce an error of 1 order of magnitude in the dust related n_{INP} estimations (U17-imm and D15) and 1/2 order of magnitude in the non-dust related estimations of D10. The same error (1/2 order of magnitude) is induced in the U17-imm(soot) (for T < -18°C). For deposition mode, a $5°$ error in the assumed T can introduce an error of 1/2 order of magnitude in the dust related n_{INP} estimations (U17-dep(dust) and S15). For the U17-dep(soot) estimates, and at T > - 45°C, the error in the assumed T has a
15 significant impact in the n_{INP} product (e.g. 1 order of magnitude between T = -45 and -40°C). On the contrary, at T < -45°C, the error in the assumed T has less impact in the final n_{INP} product (between 100% and 200% for $5°$ T error).

Regarding deposition nucleation, a big variability on the onset saturation ratio is observed in laboratory experiments of different studies, with ss_i to vary for example at -40°C between 1 and 1.5 (Hoose and Möhler, 2012). In Figure 1, we see the effect of the ss_i on the estimated n_{INP}. In S15, n_{INP} increase by 1 order of magnitude for 0.1 increase in the ss_i. In U17-
20 dep(dust), 3 orders of magnitude n_{INP} range is observed at -30°C for ss_i between 1.05 and 1.4. The range is wider at lower temperatures (4 orders at -50°C). In U17-dep(soot), 4 orders of magnitude n_{INP} range is observed at T < -40°C for ss_i between 1.05 and 1.3. This variability provide an indication of the error induced in the lidar estimated n_{INP} product due to the error in the selected ss_i. In the n_{INP} profiles discussed in Section 4.3, ss_i= 1.15 is assumed (bold line here) which could introduce up to 2 order of magnitude error if the representative ss_i for this case is between 1.05 and 1.4.

25 **3   Instruments and methodology**

The "INUIT-BACCHUS-ACTRIS" campaign in April 2016 was organized within the framework of the projects Ice Nuclei Research Unit (INUIT; https://www.ice-nuclei.de/the-inuit-project/), Impact of Biogenic versus Anthropogenic emissions on Clouds and Climate: towards a Holistic UnderStanding (BACCHUS; http://www.bacchus-env.eu/) and Aerosols, Clouds, and Trace gases Research InfraStructure (ACTRIS; https://www.actris.eu/) and focused on aerosols, clouds and ice nucleation
30 within dust-laden air over the Eastern Mediterranean. Although dust was the main component observed, other aerosol types were present as well such as soot and continental aerosols.

The atmospheric measurements conducted during the campaign included remote-sensing with aerosol lidar and sun pho- tometers as well as in-situ particle sampling with two unmanned aerial vehicles (UAV). The UAV provided observations of

the INP abundance in the lower troposphere and they were operated from the airfield of the Cyprus Institute at Orounda (35°05'42"N, 33°04'53"E, 327 m asl, about 21 km west of Nicosia) (Schrod et al., 2017). An Aerosol Robotic Network (AERONET, Holben et al. 1998) sun photometer and several in-situ instruments were operated at the Cyprus Atmospheric Observatory of Agia Marina Xyliatou (35°02'19"N, 33°03'28"E, 532 m asl, another 7 km to the west). Continuous ground-

5 based lidar observations were performed at Nicosia (35°08'26"N, 33°22'52"E, 181 m asl) with the EARLINET PollyXT multi-wavelength Raman lidar of the National Observatory of Athens (NOA). For the second half of the campaign the lidar observations were complemented at Nicosia by a sun/lunar photometer whose data were used to check the homogeneity of aerosol loading between the different sites of Nicosia and Agia Marina.

3.1 Lidar measurements

10 The EARLINET PollyXT-NOA lidar measurements at 532 nm are used in this study for the derivation of particle optical properties and mass concentration profiles. Quicklooks of all PollyXT measurements can be found on the web page of PollyNet (Raman and polarization lidar network, http://polly.tropos.de). PollyXT operates using a Nd:YAG laser that emits light at 355, 532, and 1064 nm. The receiver features 12 channels that enable measurements of elastically (three channels) and Raman scattered light (387 and 607 channels for aerosols, 407 for water vapor) as well as depolarization state of the incoming

15 light (355 and 532 nm) and near-range measurements (two elastic and two aerosol Raman channels). More details about the instrument and its measurements are provided in Engelmann et al. (2016) and Baars et al. (2016), respectively. In brief, the nightime backscatter (b) and extinction (a) coefficient profiles at 532 nm are derived using the Raman method proposed by Ansmann et al. (1992). The daytime backscatter and extinction coefficient profiles are derived using the Klett-Fernald method (Klett, 1981; Fernald , 1984), assuming a constant value for the lidar ratio (LR). The daytime Klett profiles in Section 4.1 were

20 derived using a lidar ratio of 50 sr at 15th of April and of 40 sr at 5, 9, 21 and 22 of April and a vertical smoothing length using a sliding average of 232.5 m. The integrated extinction coefficient profiles calculated with these LRs agree well with the collocated AERONET aerosol optical depth observations. The LR values also are in agreement with the nighttime Raman measurements indicating mixtures of dust and anthropogenic/continental particles at heights between 1 and 3 km.

In this work we also use space-borne observations from the Cloud-Aerosol Lidar with Orthogonal Polarisation (CALIOP)

25 on board the Cloud-Aerosol Lidar and Infrared Pathfinder Satellite Observations (CALIPSO) satellite (Winker et al., 2009). During the campaign period CALIPSO passed over Nicosia at a distance of 5 km on 5 and 21 April 2016. Here, we use the CALIPSO L2 Version 4 (V4) aerosol profile products of 21st of April 2016 and consider only quality-assured retrievals (Marinou et al., 2017; Tackett et al., 2018).

3.2 INP retrieval from lidar measurements

30 We calculated the n_{INP} profiles from lidar measurements by first separating the lidar backscatter profile in its dust and non-dust components using the aerosol-type separation technique introduced by Shimizu et al. (2004); Tesche et al. (2009). For this method, a dust particle linear depolarization ratio of $\delta_{\text{d}} = 0.31 \pm 0.04$ (Freudenthaler et al. , 2009; Ansmann et al., 2011) and a non-dust particle linear depolarization ratio of $\delta_{\text{nd}} = 0.05 \pm 0.03$ (Müller et al., 2007; Groß et al., 2013; Baars et al., 2016;

Haarig et al., 2017) was considered. The observed particle linear depolarization ratio in between these marginal values is therefore attributed to a mixture of the two aerosol types. Then, the dust extinction coefficient (α_d) is calculated using the mean LR of 45 ± 11 sr for dust transported to Cyprus (Nisantzi et al., 2015). For the non-dust component, the extinction coefficient (α_c) is calculated using a LR of 50 ± 25 sr which is representative for non-desert continental mixtures (Mamouri and Ansmann, 2014; Baars et al., 2016; Kim et al., 2018). The profiles of $n_{250,d,dry}$, $S_{d,dry}$, $n_{250,c,dry}$ and $S_{c,dry}$ are estimated from the extinction coefficient profiles using the POLIPHON (POlarization-LIdar PHOtometer Networking) AERONET-based parameterizations proposed by Mamouri and Ansmann (2015, 2016). Table 3 provides an overview of the corresponding formulas used for the calculations. Weinzierl et al. (2009) showed that for dust environments the AERONET-derived values of S_{dry} are about 95% of the total particle surface area concentration (including particles with radius < 50 nm). This assumption has been validated against airborne in-situ observations of the particle size distribution during the SAMUM experiment in Morocco. The agreement drops to $\sim 0.85 \pm 0.10\%$ for urban environments based on ground-based in-situ measurements of particle size distributions at the urban site of Leipzig (Mamouri and Ansmann, 2016).

The steps of the procedure for obtaining the profile of $n_{250,dry}$ and $S_{c,dry}$, as described above, are illustrated in an example in Figure 2. In this example, we use the PollyXT measurements at Nicosia between 1 and 2 UTC on 21 April 2016. In the final step, the dust-related n_{INP} profiles are estimated using the ice nuclei parameterizations presented in Section 2 (Eq. (1)-(7)).

3.3 UAV in-situ measurements

Two fixed-wing UAV, the "Cruiser" and the "Skywalker", performed aerosol measurements up to altitudes of 2.5 km agl (2.85 km asl). Both UAVs were used to collect INP samples onto silicon wafers using electrostatic precipitation. The Cruiser can carry a payload of up to 10 kg and it was equipped with the multi-INP sampler PEAC (programmable electrostatic aerosol collector) (Schrod et al., 2016). Skywalker X8 (a light UAV that can carry a payload of 2 kg) was equipped with a custom-built, lightweight version of a single-sampler PEAC (Schrod et al., 2017). In total, 42 UAV INP flights were performed to collect 52 samples on 19 measurement days: 7 Cruiser flights with a total of 17 samples during 6 days and 35 Skywalker flights with a total of 35 samples during 16 days.

The INP samples were subsequently analyzed with the FRIDGE INP counter (Schrod et al., 2016, 2017). FRIDGE is an isostatic diffusion chamber. The typical operation of FRIDGE allows for measurements at temperatures down to -30°C and relative humidity with respect to water (RH_w) up to water supersaturation. FRIDGE was originally designed to address the condensation and deposition freezing ice nucleation modes at water saturation and below. However, because condensation already begins at sub-saturation, its measurements at RH_w between 95% and 100% encompass ice nucleation by deposition nucleation plus condensation/immersion freezing, which cannot be distinguished by this measurement technique. Recent measurements during a big-scale inter-comparison experiment with controlled laboratory settings show, that the method compares well to other INP counters for various aerosol types (DeMott et al., 2018). However, sometimes FRIDGE measurements were on the lower end of observations when compared to instruments that encompass pure immersion freezing. The INP samples collected on 5, 15 and 21 April 2016 were used for the comparison to the lidar-derived n_{INP}. The samples were analyzed at $-20\,°C$, $-25\,°C$ and $-30\,°C$ and at RH_w of 95%, 97%, 99% and 101% with respect to water, or equivalently with respect

Atmospheric
Chemistry
and Physics
Discussions

to ice (RH_{ice}) 115% to 135% (Schrod et al., 2017). Hereon, the samples analyzed at $RH_w < 100\%$ are used as a reference for the deposition mode parameterizations and the samples analyzed at RH_w of 101% are used as a reference for the immersion/condensation parameterizations. The errors of the INP measurements were estimated to be ∼20% considering the statistical reproducibility of an individual sample, for the samples analyzed for the experiment.

5   Cruiser was additionally equipped with an optical particle counter (OPC, Met One Instruments, Model 212 Profiler) that measures the aerosol particle number concentration with 1 Hz resolution in eight channels ranging from 0.15 to 5 μm in radius (Mamali et al., 2018). The inlet of the OPC was preheated to keep the relative humidity below 50% to minimize the influence of water absorption onto particles. The Cruiser-OPC measurements on 5, 9, 15 and 22 April 2016 were used to calculate the $n_{250,dry}$ profiles discussed in Section 4.1.

10   The measurements from the OPC onboard the UAV were validated at the ground, using a similar OPC that was used for the aircraft measurements and a Differential Mobility Analyzer (DMA). From the first comparison we saw that the data have large uncertainties (underestimation) for the bin with radius 1.5 μm to 2.5 μm and for the last bin with radius more than 5 μm. From the second comparison we see that the OPC underestimates by less than 10% the number concentration of particles with radius between 0.15 μm and 0.5 μm than the DMA instrument (Burkart et al., 2010). Moreover, there are no data provided for

15   particles with radius less than 0.15 μm. In order to correct for this under-sampling we fit a bimodal number size distribution on the in-situ data and derive a corrected $n_{250,dry}$ and S_{dry}. An example of this correction is shown in Figure 3 for the number and surface size distribution measured at 1.2 km on 5 April 2016. From this analysis, and for the cases discussed in this work (Section 4.1), we found that the corrected $n_{250,dry}$ in-situ values were ∼20% higher than the raw measurements.

4   Results and discussion

20   We present here results from three UAV flights conducted during moderate dust/continental presence under cloud-free conditions and one flight conducted during an intense dust layer under cloudy conditions. The UAV OPC observations are compared to the lidar-derived n_{250} (Section 4.1). Additionally, we present the UAV-INP measurements during three days with moderate dust load conditions. From a total of six samples, five samples are collected during 5 and 15 of April under cloud-free conditions and one is collected during 21 of April under cloudy conditions. These observations are also compared to the lidar-derived

25   n_{INP} estimates (Section 4.2).

Figure 4 provides an overview of the times and heights of the PollyXT and CALIPSO lidar measurements, along with the UAV measurements, between 20 and 22 April 2016. During that period atmospheric conditions supported the transport of dust from the Saharan desert and the Arabian Peninsula to Eastern Mediterranean (Floutsi , 2018). Both plumes merged over Cyprus, with the Saharan dust plume having the bigger load and a total particle linear depolarization ratio of $\delta_p = 0.28 \pm 0.03$.

30   The elevated dust plume arrived over the lidar site at 4-5 km height at around 15 UTC on 20 April 2016, quickly widened to stretch from 2 to 8 km height with the top of the main plume at 5 km height, and disappeared at 18 UTC on 21st of April. On that day, ice clouds formed within the dust plume and were present between 02:00 and 10:45 UTC above Nicosia. Shortly after that time, at 11:01 UTC, CALIPSO over-passed the station. A second transported dust plume was observed between 03:00 and

10:00 UTC on 22 April 2016, as a homogeneous elevated layer at 1 to 2 km altitude above the lidar station. The layer consisted of a mixture of dust with pollution aerosol and is characterized by a total particle linear depolarisation ratio of $\delta_p = 0.17 \pm 0.03$. As shown in the figure, UAV flights were performed in the dust layer on 21 April 2016 (OPC measurements and INP sampling) and in the mixed layer on 22 April 2016 (INP sampling).

5   Because the OPC and INP samples have been collected at a location about 28 km to the west of the lidar site, the atmospheric homogeneity of the two areas had to be considered to select suitable measurement times for the comparisons. For that we considered sun photometer measurements at Agia Marina and Nicosia, backward trajectories, model fields and Moderate Resolution Imaging Spectroradiometer (MODIS) measurements. This was especially necessary for the case on 21 of April when clouds were formed at the top of the dust layer. During that day, the CALIPSO-derived n_{INP} at 11:01 UTC were compared

10 to UAV-measured n_{INP} acquired approximately one and a half hours earlier (between 8:30 and 9:40 UTC). The space/time homogeneity of the CALIPSO-derived s_{dry} and $n_{250,dry}$ profiles (acquired shortly after the end of the cloudy period) is confirmed by the respective estimates from the PollyXT measurements during 1 to 2 UTC (before the beginning of the cloud formation) as shown in Figure 5. The different measurement times of the ground-based and spaceborne lidars are marked in Figure 4. For the CALIPSO profiles, along-track observations ± 80 km away from the lidar station are used. During that time, the dust plume

15 declined by approximately 300 m between the two time periods. Nevertheless, CALIPSO and PollyXT retrieved profiles are in agreement within their error bars within the dense dust plume for all four parameters. Aerosol conditions were less homogeneous above and below this layer (see Figure 4) causing stronger differences between the two instruments with respect to the four parameters. The comparison between the CALIPSO-derived n_{INP} and the UAV measurements from this case are discussed in Section 4.2 (see Figure 8).

20 **4.1 Evaluation of the $n_{250,dry}$ retrieval**

For the assessment of the lidar-based n_{250}-retrieval, apart from the OPC measurements on 22 April, the measurements on 5, 9 and 15 April are used. On 5 April 2016, a homogeneous elevated dust layer has been observed above the lidar station at 1.0-1.8 km from 0 to 8 UTC. At around 8 UTC, the dust started to get mixed into the developing planetary boundary layer (PBL). In the next hours until 12 UTC, only moderate variability has been observed in the lidar range-corrected signal and the volume

25 depolarization ratio (not shown). The Cruiser UAV collected samples between 11:37 and 11:57 UTC, 30 km west of the lidar site with westerly winds prevailing. Constant δ_p of around 0.15 between 0.5 and 2.5 km supports the qualitative homogeneity of the scene during this time period.

On 9 April 2016, a thick pure dust layer (with $\delta_p \approx 0.3$) is observed above the lidar station, as part of a major dust event above Cyprus between 8 to 11 April 2016. During the period of the event, ice and water clouds are frequently formed at

30 the top of the dust layer (mainly between 3 and 6 km). The mean 500-nm aerosol optical thickness at Nicosia was 0.83 with a corresponding mean Ångström exponent of 0.17 (at 440-870 nm). DREAM model and backward trajectory analysis reveals that this event originated from central Sahara, from sources ranging diagonally from northern Niger to northeastern Libya, with the dust particles being advected by southwesterly flow directly towards Cyprus, reaching the island after one day (Schrod et al., 2017). During 6:30 to 8:15 UTC, the main dust layer was located between 1 and 2.5 km with moderate variability observed

Atmospheric
Chemistry
and Physics
Discussions

in its range-corrected signal and volume depolarization ratio observations (Figure 14 in Schrod et al. (2016)). Clouds were present in the scene with their base varying between approximately 5.5 km until 7:30 UTC to 4 km afterwords. Cruiser has collected samples between 8:12 and 8:23 UTC inside the dust layer and these observations were compared with the lidar-derived profiles at 6:50-6:59 UTC. The OPC concentrations collected that day were the highest observed during the period of

5 the INUIT-BACCHUS-ACRTIS experiment.

On 15 April 2016, a persistent dust layer that extended from approximately 2.5 km up to 7.0 km height was observed by the lidar. The 500-nm aerosol optical thickness at Nicosia increased from 0.27 at 4:20 UTC to 0.53 at 11 UTC. Backward trajectory analysis (not shown) reveals that this dust event originated from Algeria and that the dust plume was transported over Greece and Turkey before reaching Cyprus. Between 0 and 3 UTC the dust layer was located above 2 km height. From

10 the early morning hours (7 UTC) to early afternoon (14 UTC) when the boundary layer was still developing, the dust layer was confined at altitudes above 1.0 to 1.5 km. After the collapse of the boundary layer the dust layer started to descend and finally reached the ground at 18 UTC. During this day, Cruiser has collected samples between 6:54 and 8:45 UTC during the boundary layer development. A pure dust layer (with $\delta_p \approx 0.3$) was present between 2.5 and 3.8 km height. Below 2.0 km height the dust was mixed with spherical particles from the residual layer with δ_p decreasing with height and reaching 0.1 at 0.6 km. During

15 the 2-h flight, the scene above the station changed considerably, with 33% increase in the aerosol optical thickness and 15% decrease in the Ångström exponent (not shown). The UAV measurements that day reached up to 2.2 km, hence only the mixed bottom layer and the lower part of the elevated dust layer is captured by their measurements. For the comparison with the lidar-derived concentrations, only the UAV measurements inside the lower part of the elevated dust layer (> 1.7 km) are used.

The profiles of $n_{250,\mathrm{dry}}$ retrieved from PollyXT observations and in-situ measurements are shown in Figure 6 (upper panel).

20 The lidar dust-only profiles (orange lines) are calculated from the dust extinction profiles and Eq. 8 (Table 3). The remaining non-dust component is considered continental with $n_{250,\mathrm{c,dry}}$ provided by Eq. 10 (Table 3). The total $n_{250,\mathrm{dry}}$ profiles (Figure 6, upper panel, black lines) are the summation of $n_{250,\mathrm{d,dry}}$ and $n_{250,\mathrm{c,dry}}$. The red dots correspond to the uncorrected UAV $n_{250,\mathrm{dry}}$ measurements. The blue dots correspond to the corrected UAV $n_{250,\mathrm{dry}}$ measurements (as described in Section 3.3).

We have considered several additional measurements and air-transport models for properly choosing the comparison times

25 between the PollyXT and the UAV observations in order to chose scenes that are relatively homogeneous. We use only the respective height ranges at which homogeneous aerosol conditions allow for a comparison of the UAV- and lidar-derived estimates. These measurements correspond to heights above the PBL on the days 9 and 15 April (< 1 km and < 2 km respectively) and above the nocturnal boundary layer on 22 April (< 0.7km). It seams that the spatial difference has little impact on the comparison of the lidar-derived and the in-situ measured $n_{250,\mathrm{dry}}$ presented in Figure 6. In Figure 6, we see that most of the

30 in-situ-derived $n_{250,\mathrm{dry}}$ are well within the error bars of the lidar retrieval when considering the contributions of both mineral dust and continental pollution. Overall, the values of $n_{250,\mathrm{dry}}$ varied between 1 and 50 cm^{-1}.

Figure 7 provides a quantitative comparison of the observations presented in Figure 6 for lidar retrievals of $n_{250,\mathrm{dry}}$ considering both mineral dust and continental pollution and the corresponding in-situ measurements at the same height levels. Again, we see that the results agree well within the error bars of the lidar retrieval with $R^2 = 0.98$. The uncertainties of the

35 UAV-derived $n_{250,\mathrm{dry}}$ values presented in Figure 6 and Figure 7 correspond to the standard deviation of the 30 seconds average

(OPC initial resolution of 1 second). The systematic error of the OPC measurements due to the assumption of the refractive index and the shape of the particles used in the OPC retrievals, were not taken into account in this study. Nevertheless, it is not expected to be high because the refractive index used in the OPC retrievals is characteristic for dust particles (n=1.59). We have to keep in mind also the effect of some inhomogeneity between the two stations, that cannot be excluded due to the two

5 different locations of the PollyXT and the UAV observations. In view of all uncertainty sources, the lidar- and UAV- derived $n_{250,\mathrm{dry}}$ are in good agreement. In terms of absolute values, the lidar-derived $n_{250,\mathrm{dry}}$ are slightly lower than the UAV-derived ones.

The profiles of S_{dry} retrieved from PollyXT observations and in-situ measurements are shown in Figure 6 (lower panel). The dust-only profiles (orange lines) are calculated from the dust extinction profiles and Eq. 9 (Table 3). The remaining non-dust

10 component is considered continental with $n_{250,\mathrm{c,dry}}$ provided by Eq. 11 (Table 3). The total S_{dry} profiles (Figure 6, lower panel, black lines) are the summation of $S_{\mathrm{d,dry}}$ and $S_{\mathrm{c,dry}}$. These profiles are compared to the total S_{dry} derived from the corrected in-situ number size distribution (e.g. Figure 3b). We see that the latter agree well within the uncertainty of the lidar-derived $S_{\mathrm{d,dry}}$ (orange line), but do not agree well when both mineral dust and continental pollution are considered (black line). This is mainly due to the sampling cut-off of the OPC instrument for particles with radius smaller than 150 nm, affecting the correction

15 of the size distribution at these size ranges, where most of the polluted continental load should lay. The effect is not seen in the corrected n_{250}, since the sizes ranges considered there are larger than 250 nm.

4.2 Evaluation of the n_{INP} retrieval

For the assessment of the lidar-based n_{INP}-retrieval, the UAV measurements on 5, 15 and 21 April 2016 are used. The samples of 5 and 15 of April were collected under moderately mixed dust conditions, as indicated by the measured depolarization

20 values, and they were collocated with the UAV-OPC measurements shown in Figure 6. One sample was collected on 5 April from 1.823 km altitude ($\delta_{\mathrm{p}} = 0.14 \pm 0.02$) and two samples were collected on 15 April from 0.998 km and 1.281 km altitude ($\delta_{\mathrm{p}} = 0.15 \pm 0.03$). On 21 April, particles were collected from inside the dust plume at 2.55 km altitude, with $\delta_{\mathrm{p}} = 0.28 \pm 0.03$ (Figure 4). Analysis performed in FRIDGE chamber provided the INP concentrations. Moreover, after the analysis in FRIDGE, the sample of 21 April was analyzed by single particle analysis using scanning electron microscopy, which show that 99% of

25 the particles were dust and 1% was Ca sulfates and carbonaceous particles (Schrod et al., 2017).

Figure 8 shows the n_{INP} for the case of 21 April, from the lidar measurements (colored symbols) and measured from the UAV-FRIDGE samples (black triangles), (a) for deposition nucleation (as a function of saturation over ice) and (b) for condensation and immersion freezing (as a function of temperature). The in-situ samples were analyzed at $-20\,^\circ$C $-25\,^\circ$C and $-30\,^\circ$C. For the deposition nucleation (Figure 8a), the samples were analyzed at RH_{w} of 95%, 97%, and 99%, leading to three values of

30 S_{ice} for each temperature (1.16, 1.18 and 1.23 for $-20\,^\circ$C, 1.21, 1.24 and 1.26 for $-25\,^\circ$C and 1.27, 1.30 and 1.33 for $-30\,^\circ$C). For the immersion freezing (Figure 8 b), the samples were analyzed at RH_{w} of 101%, leading to S_{ice} of 1.23, 1.29 and 1.35 for the temperatures of $-20\,^\circ$C $-25\,^\circ$C and $-30\,^\circ$C respectively. When the samples were analyzed at $T = -20\,^\circ$C, $RH_{\mathrm{w}} = 101\%$ and $S_{\mathrm{ice}} = 1.23$, we refer to the freezing process as condensation freezing.

Figure 8 (a) shows that the n_{INP} derived from lidar measurements using the U17-dep agree very well with the in-situ observations within their uncertainties. Moreover, it captures the whole extend of the n_{INP} range for different ice supersaturation conditions, with values of n_{INP} spanning over 2.5 orders of magnitude. The lidar-retrieved U17-dep values in this case are dominated from the dust related n_{INP} (estimated from Eq. 3; Table 1), as the non-dust related n_{INP} (estimated from Eq. 6;

5 Table 1) are five orders of magnitude lower. The S15 parameterization produces n_{INP} values which are 3-4 orders of magnitude larger than the in-situ measurements. A big overestimation was already expected as discussed in Section 2 and Steinke et al. (2015) but for completeness we include these results.

Figure 8 (b) shows the lidar derived immersion/condensation INPs. U17-imm dust-related n_{INP} are calculated using the INP parameterization of Eq. 1 (Table 1) with the $S_{d,dry}$ from Eq. 9 (Table 3). The D15 dust-related n_{INP} are calculated using the Eq.

10 2 (Table 1) with the $n_{250,d,dry}$ from Eq. 8 (Table 3). The D10 continental-related n_{INP} are calculated using the Eq. 7 (Table 1) with the $n_{250,c,dry}$ from Eq. 10 (Table 3). The D15+D10 values for the total (dust + continental) aerosol in the scene, are the summation of the aforementioned D15 (dust-related) and D10 (continental-related) n_{INP} calculations (See Figure A1 and A2 in Appendix). We did not include the U17-imm soot estimates in the plot since these are quite similar to the estimated values from D10 at temperatures < -18°C (Section 2; Figure 1). Consequently, for the total INP load in the scene, the estimations

15 provided from the D15+D10 are similar to the ones provided from D15+U17-imm(soot). In the rest of this manuscript, we will discuss only the joint D15+D10 retrievals, keeping in mind that the same conclusions apply for the joint D15+U17-imm(soot) retrieval.

The lidar-derived n_{INP} using D15 for dust and D10 for continental particles are in very good agreement with the in-situ observations, within the respective uncertainties. A very close agreement is shown for the sample analyzed under condensation

20 freezing conditions (at -20°C): the in-situ sample contained $3.6\pm0.1\,\mathrm{L}^{-1}$ and the lidar observations using D15+D10 provided values of $3.8\,\mathrm{L}^{-1}$ for dust and $2.4\,\mathrm{L}^{-1}$ for non-dust/continental particles. The U17-imm provides n_{INP} values which are larger than the values provided by D15+D10 by one order of magnitude, but the agreement with the in-situ observations is still good within the uncertainty of the parameterization. At T=-25°C, the in-situ n_{INP} ($12 \pm 3\,\mathrm{L}^{-1}$) is within the error bars of the concentration derived with D15+D10 ($26\,\mathrm{L}^{-1}$ with a negative error of $14\,\mathrm{L}^{-1}$) and 1.5 orders of magnitude lower than the

25 concentration derived with U17-imm. The contribution from the non-dust INP (D10 or U17-imm(soot)) is insignificant, with values that are one order of magnitude lower than the n_{INP} provided by D15. At T=-30°C, the in-situ n_{INP} is $62 \pm 14\,\mathrm{L}^{-1}$ while D15+D10 n_{INP} estimates are one order of magnitude higher ($242\,\mathrm{L}^{-1}$) and U17-imm are two orders of magnitude higher ($8670\,\mathrm{L}^{-1}$).

Figure 9 shows scatter plots of the lidar-estimated n_{INP} from all the analyzed cases (dust dominated and moderately mixed

30 cases) against the in-situ observations for (a) deposition nucleation and (b) condensation and immersion freezing. In (c) the ratio between the lidar-derived and the in-situ n_{INP} is provided, for condensation and immersion freezing. Figure 9 (a) shows that the calculations from U17-dep are in excellent agreement with the in-situ observations, with 97% of the in-situ n_{INP} to be within the error bars of the lidar retrievals and within a factor of 10 around the 1:1 line (r=0.75). The n_{INP} sampled with the UAVs ranged between 0.02 and $20\,\mathrm{L}^{-1}$. Using S15 parameterization, the predicted n_{INP} are 3 to 5 orders of magnitude higher

35 that the measurements (r=0.42).

Atmospheric
Chemistry
and Physics
Discussions

Figure 9 (b and c) shows that U17-imm provides n_{INP} values that are overall 1 to 3 orders of magnitude higher than the in-situ. In particular they are 3-11, 2-80 and 2-1000 times larger than the samples analyzed at FRIDGE chamber at $-20\,°\mathrm{C}$, $-25\,°\mathrm{C}$ and $-30\,°\mathrm{C}$, respectively. On the contrary, in 85% of the analyzed cases D15+D10 lidar retrievals are less than a factor of 10 higher than the measurements. Especially for the samples analyzed under condensation freezing conditions, the D15+D10

5   estimated n_{INP} were from equal to up to 2.5 times higher than the in-situ. Larger differences are observed at the temperatures where immersion freezing dominates over condensation as the main INP pathway, with 1.5-7 times larger values at $-25\,°\mathrm{C}$ and 4-13 times larger values at $-30\,°\mathrm{C}$. As shown in DeMott et al. (2018), recent comparisons of n_{INP} derived from samples analyzed in FRIDGE chamber usually present good linear correlations but somewhat lower values with observations derived from pure immersion paths. Possible reasons for these discrepancies may be (a) deficits and inadequacies in instrumentation

10   and measurement techniques, (b) the lacking overlap of the freezing modes, (c) inconsistencies between the inlet systems of the parameterization measurement (using cutoffs) and the in-situ measurements (using no cutoff) and (d) a variation in RH_{w} (D15: 105%; FRIDGE: 101%) (Schrod et al., 2017).

The error bars of the lidar-based n_{INP} estimations in Figure 8 and Figure 9 are calculated using Gaussian error propagation together with the typical uncertainties provided in Table 2. In DeMott et al. (2015), a standard deviation of two orders of

15   magnitude is reported as the uncertainty of the D15 parameterization. In the same plots, the uncertainty of the n_{INP} from in-situ data is very low. Under most experimental conditions, the repeatability of the ice nucleation in the FRIDGE chamber dominates other uncertainties. An uncertainty of 20% has been suggested as a useful guideline for the uncertainty of the intrinsic measurements, corresponding to the statistical reproducibility of an individual sample. However, it has also been reported that natural variability by far outweighs the intrinsic uncertainty (Schrod et al., 2016). We need to consider the full uncertainty

20   including precision and accuracy. The DeMott et al. (2018) inter-comparison of INP methods saw that, at all temperatures and for various test aerosols, the n_{INP} uncertainty for immersion freezing is one order of magnitude, while for deposition condensation the uncertainty is expected to be even larger.

Our analysis suggests that the D15+D10 (and D15+U17-imm(soot)) immersion/condensation parameterization (applicable for the temperature range -35 °C to $-9\,°\mathrm{C}$) and the U17-dep parameterization (applicable for the temperature range $-50\,°\mathrm{C}$

25   to $-33\,°\mathrm{C}$) agree well with in-situ observations of n_{INP} and can provide good n_{INP} estimates in dust-dominated environments. The U17-imm pure immersion parameterization provides 1-2 orders of magnitude larger values, we therefore consider the n_{INP} estimates according to D15+D10 as the lower boundary of possible values, with the actual values to be up to one order of magnitude larger in the temperature regime of immersion freezing.

4.3 n_{INP} profiles from PollyXT and CALIOP before and after cloudy observations

30   The case study of 21 April 2016 (Figure 4) demonstrates the feasibility of the proposed methodology to provide profiles of cloud-relevant aerosol parameters up to the cloud levels, using (ground-base and space-borne) lidar measurements. In particular for this case, the temporarily averaged PollyXT lidar observations at 1-2 UTC and the spatially averaged CALIPSO observations at 11:01 UTC provide us the information of the $n_{250,\mathrm{dry}}$, S_{dry} and n_{INP} right before and after the cloud event which was formed inside the dust layer that day between 02:00 and 10:45 UTC. The profiles of $n_{250,\mathrm{dry}}$ and S_{dry} before (PollyXT) and

Atmospheric
Chemistry
and Physics
Discussions

after (CALIPSO) the cloud event are the ones already presented in Figure 5. As discussed above, the dust plume declined by approximately 300 m during that period while its n_{INP} stayed relatively constant inside its dense part. On the contrary, above the main dust layer the aerosol conditions are different, with multiple thin layers up to 8 km altitude only before the appearance of the clouds. Specifically, a constant contribution of non-dust/continental particles is observed between 5.6 and 8 km ($n_{250,dry}$

5 = 0.4 ± 0.2 cm^{-3}; Figure 5 (d)) and three thin dust layers are visible at 6.4, 6.8 and 7.8 km with dust $n_{250,dry}$ of 2.9, 1.5 and 2.0 cm^{-3}, respectively, and a local minimum at 7.55 km (0.01 cm^{-3}) (Figure 5 (c)). The n_{INP} concentrations of these instances derived from the different parameterizations at altitudes between 3 and 8 km are presented in Figure 10.

Figure 10 (a) shows that before the cloud formation the non-dust aerosols contribute to a gradual increase of n_{INP} per height from 0.04 L^{-1} (4.5 km; -10 °C) up to 0.4 L^{-1} (5.8 km; -20 °C) and 4 L^{-1} (7.8 km; -34 °C) (based on D10). Using U17-imm

10 for soot we derived the n_{INP} for the relevant non-dust particles of 10^{-4} L^{-1} (-10 °C), 0.04 L^{-1} (-20 °C) and 8 L^{-1} (-34 °C). Figure 10 (a) shows here again the relatively good agreement between the lidar-derived non-dust n_{INP} using D10 and U17-imm parameterizations at T< -20 °C and their significant discrepancies at lower temperatures. The dust aerosols in the scene contribute to a gradual increase of n_{INP} inside the main dust layer from 0.05 L^{-1} (4.5 km; -10 °C) to 0.4 L^{-1} (5.3 km; -14 °C). Then a decrease of one order of magnitude is observed up to 6 km (0.06 L^{-1}; -20 °C) at the top end of the main dust layer.

15 Above this altitude, a wavy n_{INP} profile is observed with local maximal at 6.5, 7.0 and 7.9 km of 2 L^{-1} (-22 °C), 4 L^{-1} (-25 °C) and 200 L^{-1} (-33 °C). The aforementioned values correspond to D15 estimates. The U17-imm dust estimates in this case are 60 L^{-1} (-22 °C), 200 L^{-1} (-25 °C) and 1000 L^{-1} (-33 °C). Overall, 91% of the total n_{INP} is attributed to dust aerosols (D15) and 9% to non-dust/continental aerosols (D10) at altitudes between 6.3-8 km (Temperatures < -21 °C). These abundances are reversed inside the main dust layer (altitudes between 4-5.5 km; Temperatures [-20,-6] °C) where 34% of the total n_{INP} is

20 attributed to dust aerosols (0.06 L^{-1}) and 66% to non-dust/continental aerosols (0.12 L^{-1}). Shortly after the period analyzed here, mixed phase clouds are observed above Nicosia at first at altitudes between 5-7 km and during the rest of the cloudy period mainly above 4 km (Figure 4).

Figure 10 (b) show the lidar-derived n_{INP} shortly after the end of the cloudy conditions. At that time, the main dust layer is observed at altitudes up to 5.6 km without additional layers above it. As these observations are close to the local noon, the

25 air temperature above the station has increased by 7 degrees, leading to temperatures of 0 °C at 3.8 km and -15 °C at 5.6 km. At these altitudes, a relatively constant contribution of non-dust/continental particles was present ($n_{250,dry}$ = 0.4 ± 0.2 cm^{-3}; Figure 5 (d)) which led to a gradually increase of the non-dust n_{INP} per height from 2x10^{-4} L^{-1} (4 km; -1 °C) to 10^{-2} L^{-1} (4.4 km; -4 °C) to 0.2 L^{-1} (5.3 km; -15 °C) (D10 estimates). Additionally, the dust concentration per altitude was constant inside the dust layer and is decreased gradually above 4.6 km ($n_{250,dry}$ = 16 cm^{-3}; 4 - 4.6 km); Figure 5 (c)). The dust-related

30 n_{INP} per height are 8x10^{-3} L^{-1} (4 km; -1 °C), 3x10^{-3} L^{-1} (4.4 km; -4 °C) and 0.1 L^{-1} (5.3 km; -12 °C) (D10 estimates). Overall, 25% of the total n_{INP} is attributed to dust aerosols (D15) and 75% to non-dust/continental aerosols (D10) at altitudes between 3.8-5.6 km.

The n_{INP} before and after the cloud development was 0.6 L^{-1} and 0.1 L^{-1} respectively at 5.3 km altitude (D15+D10 in Figure 5). This difference is due to the increase of the air temperature during the day and the decrease of $n_{250,dry}$ and S_{dry}.

35 Before the cloud formation, the n_{INP} values at [6,7.5] km were one order of magnitude larger (3 L^{-1}) and at 7.8 km were two

orders of magnitude higher ($200\,\mathrm{L}^{-1}$). These results indicate that the particles in the main dust layer and the thin layers above it acted as seeding INPs for the cloud that formed in that layer, affecting also its characteristics, and thus has been removed from the INP reservoir. However, further measurements would be necessary to reach a more concrete conclusion, as for example, measurements of the atmosphere dynamics (e.g. from a wind lidar), and observations of the 3D evolution of the cloud (e.g.

5   from a cloud radar). Nevertheless, the results are in agreement with the current hypothesizes concerning ice formation in clouds via INP use (het. ice formation).

5   Summary and conclusions

We present a methodology for deriving n_{INP} profiles from lidar measurements and its comparison to in-situ UAV measurements. More specifically, seven INP parameterizations were tested to obtain lidar (ground-based and space-borne) n_{INP} estimates rep-

10   resentative of mineral dust and continental/pollution/soot aerosol. We proved that a compilation of the parameterizations of DeMott et al. (2015) (D15) and DeMott et al. (2010) (D10) for dust and non dust particles respectively is in good agreement with airborne in-situ measurements (Schrod et al., 2017) for addressing immersion/condensation freezing (at T>$-35\,^{\circ}$C). Same conclusion is derived from the compilation of the parameterizations of DeMott et al. (2015) (D15) for dust and Ullrich et al. (2017) (U17) for soot. Specifically, lidar-derived n_{INP} using D15+D10 (and D15+U17-imm(soot)) agree with the in-situ mea-

15   surements within the reported uncertainty range of the D15 parameterization (i.e., two orders of magnitude; DeMott et al. (2015)). The best assessment for the deposition-related INPs was derived with the Ullrich et al. (2017) deposition nucleation parameterization for dust and soot (for T<$-33\,^{\circ}$C), with results agreeing with the UAV-FRIDGE measurements within one order of magnitude for different values of ice supersaturation.

    The cloud-relevant aerosol parameters necessary for INP estimations ($n_{250,\mathrm{dry}}$ and S_{dry}) were derived from lidar measure-

20   ments as shown by Mamouri and Ansmann (2015, 2016). The comparison between the lidar-derived concentrations of dry particles with radii larger than $250\,\mathrm{nm}$ with coincident UAV-OPC in-situ measurements (Mamali et al., 2018) showed a good agreement with slightly lower values (32%) of $n_{250,\mathrm{dry}}$ by the lidar (this effect is less pronounces at low concentrations) (squared correlation coefficient of 0.98). For the majority of the cases, we found that in-situ observations and remote-sensing estimates are in good agreement within their uncertainty ranges.

25   Our methodology has been validated for cases with dust presence. Additional measurements are required in order to define the optimum INP parameterizations for non-dust atmospheric conditions (e.g. continental, marine, smoke). Future experimental INP campaigns with airborne in-situ observations from aircrafts (including UAVs) around laser beams at pure marine conditions and at mixed aerosol conditions would provide ideal set-up for an in-depth investigation of the potential of the lidar-based INP profiles in complex and non-dust atmospheric conditions.

30   The results presented in this study give us confidence to proceed to the next step which is to combine cloud-relevant lidar aerosol and wind parameters and cloud radar height-resolved observations to monitor the evolution of clouds embedded in aerosol layers. This will provide a unique opportunity to better understand aerosol-cloud-interactions in the field of heterogeneous ice formation.

Moreover, the study enhances the confidence for the production of global 3D products of $n_{250,\text{dry}}$, S_dry and n_INP from CALIPSO dataset. The application of our methodology to more than a decade-long CALIPSO measurements could provide valuable insight into global height-resolved distribution of $n_{250,\text{dry}}$ and n_INP related to mineral dust, and possibly other aerosol types. This will enable global-wide studies of aerosol cloud interactions to combine the new product with satellite radar obser-

5   vations (CloudSat) and the upcoming EarthCARE (Earth Cloud Aerosol and Radiation Explorer) mission.

A challenge of this global INP climatology will be the assessment of its underestimation at high altitudes where is known that CALIPSO observations can miss thin layers with small concentrations. A way to investigate the effect of these satellite-undetected layers in the $n_{250,\text{dry}}$, S_dry and n_INP CALIPSO products is the utilization of ground-based lidar network observations as for example EARLINET and PollyNet.

10   **Appendix A: Lidar retrievals of n_INP**

A1   Methodological diagram for the analysis of the ground-based lidar measurements

The Figure A1 illustrates the general idea of the methodology followed for the INP estimations from the PollyXT measurements. The equations for the conversions of the measured optical properties into the microphysical properties are provided in Table 3. The equations for the conversions of the microphysical properties to INPs are provided in Table 1.

15   **A2   Methodological diagram for the analysis of the space-borne lidar measurements**

The Figure A2 illustrates the general idea of the methodology followed for the INP estimations from the CALIPSO measurements. The equations for the conversions of the measured optical properties into the microphysical properties are provided in Table 3. The equations for the conversions of the microphysical properties to INPs are provided in Table 1.

Competing interests. The authors declare that they have no conflict of interest.

20   *Disclaimer.* This article is part of the special issue "EARLINET aerosol profiling: contributions to atmospheric and climate research". It is not associated with a conference.

Atmospheric
Chemistry
and Physics
Discussions

Open Access

EGU

References

Altaratz, O., Koren, I., Remer, L. A., and Hirsch, E.: Review: Cloud invigoration by aerosols—Coupling between microphysics and dynamics, Atmos. Res., 140, 38-60, doi:10.1016/j.atmosres.2014.01.009, 2014.

Amiridis, V., Wandinger, U., Marinou, E., Giannakaki, E., Tsekeri, A., Basart, S., Kazadzis, S., Gkikas, A., Taylor, M., Baldasano, J., and

5   Ansmann, A.: Optimizing CALIPSO Saharan dust retrievals, Atmos. Chem. Phys., 13, 12089-12106, https://doi.org/10.5194/acp-13-12089-2013, 2013.

Ansmann, A., Wandinger, U., Riebesell, M., Weitkamp, C., Michaelis, W. Independent measurement of extinction and backscatter profiles in cirrus clouds by using a combined raman elastic-backscatter lidar, Applied Optics, 31 (33), pp. 7113-7131. DOI: 10.1364/AO.31.007113, 1992.

10   Ansmann, A., I. Mattis, D. Muller, U. Wandinger, M. Radlach, D. Althausen, and R. Damoah: Ice formation in Saharan dust over central Europe observed with temperature/humidity/aerosol Raman lidar, J. Geophys. Res., 110, D18S12, doi:10.1029/2004JD005000, 2005.

Ansmann, A., Tesche, M., Seifert, P. Althausen, D. Engelmann, R. Fruntke, J. Wandinger, U. Mattis, I. and Müller, D.: Evolution of the ice phase in tropical altocumulus: SAMUM lidar observations over Cape Verde, J. Geophys. Res., 114, D17208, doi: 10.1029/2008JD011659, 2009.

15   Ansmann, A., Tesche, M., Seifert, P., Groß, S., Freudenthaler, V., Apituley, A., Wilson, K. M., Serikov, I., Linné, H., Heinold, B., Hiebsch, A., Schnell, F., Schmidt, J., Mattis, I., Wandinger, U., and Wiegner, M.: Ash and fine-mode particle mass profiles from EARLINET-AERONET observations over central Europe after the eruptions of the Eyjafjallajökull volcano in 2010, J. Geophys. Res. - Atmos., 116, 2011.

Ansmann, A., Seifert, P., Tesche, M., and Wandinger, U.: Profiling of fine and coarse particle mass: case studies of Saharan dust and

20   Eyjafjallajökull/Grimsvötn volcanic plumes, Atmos. Chem. Phys., 12, 9399-9415, doi:10.5194/acp-12-9399-2012, 2012.

Baars, H., Kanitz, T., Engelmann, R., Althausen, D., Heese, B., Komppula, M., Preißler, J., Tesche, M., Ansmann, A., Wandinger, U., Lim, J.-H., Ahn, J. Y., Stachlewska, I. S., Amiridis, V., Marinou, E., Seifert, P., Hofer, J., Skupin, A., Schneider, F., Bohlmann, S., Foth, A., Bley, S., Pfüller, A., Giannakaki, E., Lihavainen, H., Viisanen, Y., Hooda, R. K., Pereira, S. N., Bortoli, D., Wagner, F., Mattis, I., Janicka, L., Markowicz, K. M., Achtert, P., Artaxo, P., Pauliquevis, T., Souza, R. A. F., Sharma, V. P., van Zyl, P. G., Beukes, J. P., Sun, J., Rohwer,

25   E. G., Deng, R., Mamouri, R.-E., and Zamorano, F.: An overview of the first decade of PollyNET: An emerging network of automated Raman-polarization lidars for continuous aerosol profiling, Atmos. Chem. Phys., 16, 5111-5137, doi:10.5194/acp-16-5111-2016, 2016.

Barahona, D. and Nenes, A.: Parameterizing the competition between homogeneous and heterogeneous freezing in cirrus cloud formation – monodisperse ice nuclei, Atmos. Chem. Phys., 9, 369-381, doi:0.5194/acp-9-369-2009, 2009.

Bègue, N., Tulet, P., Pelon, J., Aouizerats, B., Berger, A., and Schwarzenboeck, A.: Aerosol processing and CCN formation of an intense

30   Saharan dust plume during the EUCAARI 2008 campaign, Atmos. Chem. Phys., 15, 3497-3516, doi:10.5194/acp-15-3497-2015, 2015.

Bühl, J., Seifert, P., Myagkov, A., and Ansmann, A.: Measuring ice- and liquid-water properties in mixed-phase cloud layers at the Leipzig Cloudnet station, Atmos. Chem. Phys., 16, 10609-10620, https://doi.org/10.5194/acp-16-10609-2016, 2016.

Burkart, J.,Steiner, G., Reischl, G., Moshammer, H.,Neuberger, M. and Hitzenberger, R.: Characterizing the performance of two optical particle counters (Grimm OPC1.108 and OPC1.109) under urban aerosol conditions, Journal of Aerosol Science, Volume 41, Issue 10,

35   Pages 953-962, ISSN 0021-8502, doi:https://doi.org/10.1016/j.jaerosci.2010.07.007, 2010.

Atmospheric
Chemistry
and Physics
Discussions

Burkert-Kohn, M., Wex, H., Welti, A., Hartmann, S., Grawe, S., Hellner, L., Herenz, P., Atkinson, J. D., Stratmann, F., and Kanji, Z. A.: Leipzig Ice Nucleation chamber Comparison (LINC): Intercomparison of four online ice nucleation counters, Atmos. Chem. Phys., 17, 11683-11705, doi:10.5194/acp-17-11683-2017, 2017.

de Boer, G., Morrison, H., Shupe, M. D., and Hildner, R.: Evidence of liquid dependent ice nucleation in high-latitude stratiform clouds from surface remote sensors, Geophys. Res. Lett., 38, L01803, doi:10.1029/2010GL046016, 2011.

DeMott, P. J., Prenni, A. J., Liu, X., Kreidenweis, S. M., Petters, M. D., Twohy, C. H., Richardson, M. S., Eidhammer, T., and Rogers, D. C.: Predicting global atmospheric ice nuclei distributions and their impacts on climate, P. Natl. Acad. Sci., 107, 11217–11222, doi:10.1073/pnas.0910818107, 2010.

DeMott, P. J., Prenni, A. J., McMeeking, G. R., Sullivan, R. C., Petters, M. D., Tobo, Y., Niemand, M., Möhler, O., Snider, J. R., Wang, Z., and Kreidenweis, S. M.: Integrating laboratory and field data to quantify the immersion freezing ice nucleation activity of mineral dust particles, Atmos. Chem. Phys., 15, 393–409, doi:10.5194/acp-15-393-2015, 2015.

DeMott, P. J., Hill, T. C. J., McCluskey, C. S., Prather, K. A., Collins, D. B., Sullivan, R. C., Ruppel, M. J., Mason, R. H., Irish, V. E., Lee, T., Hwang, C. Y., Rhee, T. S., Snider, J. R., McMeeking, G. R., Dhaniyala, S., Lewis, E. R., Wentzell, J. J. B., Abbatt, J., Lee, C., Sultana, C. M., Ault, A. P., Axson, J. L., Martinez, M. D., Venero, I., Santos-Figueroa, G., Stokes, M. D., Deane, G. B., Mayol-Bracero, O. L., Grassian, V. H., Bertram, T. H., Bertram, A. K., Moffett, B. F., and Franc, G. D.: Sea spray aerosol as a unique source of ice nucleating particles, P. Natl. Acad. Sci., doi:10.1073/pnas.1514034112, Early Edition, 2015b.

DeMott, P. J., Hill, T. C. J., Petters, M. D., Bertram, A. K., Tobo, Y., Mason, R. H., Suski, K. J., McCluskey, C. S., Levin, E. J. T., Schill, G. P., Boose, Y., Rauker, A. M., Miller, A. J., Zaragoza, J., Rocci, K., Rothfuss, N. E., Taylor, H. P., Hader, J. D., Chou, C., Huffman, J. A., Pöschl, U., Prenni, A. J., and Kreidenweis, S. M.: Comparative measurements of ambient atmospheric concentrations of ice nucleating particles using multiple immersion freezing methods and a continuous flow diffusion chamber, Atmos. Chem. Phys., 17, 11227-11245, doi:10.5194/acp-17-11227-2017, 2017.

DeMott, P. J., Möhler, O., Cziczo, D. J., Hiranuma, N., Petters, M. D., Petters, S. S., Belosi, F., Bingemer, H. G., Brooks, S. D., Budke, C., Burkert-Kohn, M., Collier, K. N., Danielczok, A., Eppers, O., Felgitsch, L., Garimella, S., Grothe, H., Herenz, P., Hill, T. C. J., Höhler, K., Kanji, Z. A., Kiselev, A., Koop, T., Kristensen, T. B., Krüger, K., Kulkarni, G., Levin, E. J. T., Murray, B. J., Nicosia, A., O'Sullivan, D., Peckaus, A., Polen, M. J., Price, H. C., Reicher, N., Rothenberg, D. A., Rudich, Y., Santachiara, G., Schiebel, T., Schrod, J., Seifried, T. M., Stratmann, F., Sullivan, R. C., Suski, K. J., Szakáll, M., Taylor, H. P., Ullrich, R., Vergara-Temprado, J., Wagner, R., Whale, T. F., Weber, D., Welti, A., Wilson, T. W., Wolf, M. J., and Zenker, J.: The Fifth International Workshop on Ice Nucleation phase 2 (FIN-02): Laboratory intercomparison of ice nucleation measurements, Atmos. Meas. Tech. Discuss., https://doi.org/10.5194/amt-2018-191, in review, 2018.

Dusek, U., Frank, G. P., Hildebrandt, L., Curtius, J., Schneider, J., Walter, S., Chand, D., Drewnick, F., Hings, S., Jung, D., Borrmann, S., and Andreae M. O.: Size matters more than chemistry for cloud-nucleating ability of aerosol particles, Science, 1375-1378, doi:10.1126/science.1125261, 2006.

Engelmann, R., Kanitz, T., Baars, H., Heese, B., Althausen, D., Skupin, A., Wandinger, U., Komppula, M., Stachlewska, I. S., Amiridis, V., Marinou, E., Mattis, I., Linné, H., and Ansmann, A.: The automated multiwavelength Raman polarization and water-vapor lidar PollyXT: The neXT generation, Atmos. Meas. Tech., 9, 1767-1784, doi:10.5194/amt-9-1767-2016, 2016.

Fernald, F. G.: Analysis of atmospheric lidar observations: some comments, Appl. Opt. 23, 652-653, https://doi.org/10.1364/AO.23.000652, 1984.

Floutsi, A.: Determination of aerosol optical properties with lidar. A comparison between algorithms, (Master thesis), TU Delft, uuid:6c012d93-4df8-49be-8b04-e09196ba7a37, 2018.

Freudenthaler, V., Esselborn, M., Wiegner, M., Heese, B., Tesche, M., Ansmann, A., Müller, D., Althausen, D., Wirth, M., Fix, A., Ehret, G., Knippertz, P., Toledano, C., Gasteiger, J., Garhammer, M., and Seefeldner, M.: Depolarization ratio profiling at several wavelengths in pure Saharan dust during SAMUM 2006, Tellus B, 61, 165–179, doi:10.1111/j.1600-0889.2008.00396.x, 2009.

Garimella, S., Huang, Y.-W., Seewald, J. S., and Cziczo, D. J.: Cloud condensation nucleus activity comparison of dry- and wet-generated
mineral dust aerosol: The significance of soluble material, Atmos. Chem. Phys., 14, 6003-6019, doi:10.5194/acp-14-6003-2014, 2014.

Haarig, M., Ansmann, A., Gasteiger, J., Kandler, K., Althausen, D., Baars, H., Radenz, M., and Farrell, D. A.: Dry versus wet marine particle optical properties: RH dependence of depolarization ratio, backscatter, and extinction from multiwavelength lidar measurements during SALTRACE, Atmos. Chem. Phys., 17, 14199-14217, https://doi.org/10.5194/acp-17-14199-2017, 2017.

Großﬂ, Esselborn M, Abicht F, Wirth M, Fix A, Minikin A.: Airborne high spectral resolution lidar observation of pollution aerosol during
EUCAARI-Longrex, Atmos. Chem. Phys., 13, 2435-2444, https://doi.org/10.5194/acp-13-2435-2013, 2013.

Holben, B. N., Eck, T. F., Slutsker, I., Tanré, D., Buis, J. P., Setzer, A., Vermote, E., Reagan, J. A., Kaufman, Y. J., Nakajima, T., Lavenu, F., JankowiakI., and Smirnov, A.: AERONET—A federated instrument network and data archive for aerosol characterization, Rem. Sens. Environ., 66, 1-16, doi:10.1016/S0034-4257(98)00031-5, 1998.

Hoose, C. and Möhler, O.: Heterogeneous ice nucleation on atmospheric aerosols: A review of results from laboratory experiments, Atmos.
Chem. Phys., 12, 9817-9854, doi:10.5194/acp-12-9817-2012, 2012.

Illingworth, A. J., Hogan, R. J., O'Connor, E. J., Bouniol, D., Delanoe, J., Pelon, J., Protat, A., Brooks, M. E., Gaussiat, N., Wilson, D. R., Donovan, D. P., Klein Baltink, H., van Zadelhoff, G.-J., Eastment, J. D., Goddard, J. W. F., Wrench, C. L., Haeffelin, M., Krasnov, O. A., Russchenberg, H. W. J., Piriou, J.-M., Vinit, F., Seifert, A., Tompkins, A. M., and Willen, J., CLOUDNET: Continuos evaluation of cloud profiles in seven operational models using ground-based observations, B. Am. Meteorol. Soc., 88, 883–898, 2007.

Janjic, Z. I., Gerrity Jr., J. P., and Nickovic, S.: An Alternative Approach to Nonhydrostatic Modeling, Mon. Weather Rev., 129, 1164–1178,
2001.

Kamphus, M., Ettner-Mahl, M., Klimach, T., Drewnick, F., Keller, L., Cziczo, D. J., Mertes, S., Borrmann, S., and Curtius, J.: Chemical composition of ambient aerosol, ice residues and cloud droplet residues in mixed-phase clouds: single particle analysis during the Cloud and Aerosol Characterization Experiment (CLACE 6), Atmos. Chem. Phys., 10, 8077-8095, doi:10.5194/acp-10-8077-2010, 2010.

Kanitz, T., Seifert, P., Ansmann, A., Engelmann, R., Althausen, D., Casiccia, C., and Rohwer, E. G.: Contrasting the impact of aerosols at northern and southern midlatitudes on heterogeneous ice formation, Geophys. Res. Lett., 38, L17802, doi:10.1029/2011GL048532, 2011.

Kanji, Z. A., Ladino, L. A., Wex, H., Boose, Y., Burkert-Kohn, M., Cziczo, D. J., Krämer, M.: Overview of ice nucleating particles, Meteorological Monographs, 58, doi:10.1175/AMSMONOGRAPHS-D-16-0006.1, 2017.

Kelly, J. T., Chuang, C. C., and Wexler, A. S.: Influence of dust composition on cloud droplet formation, Atmos. Environ., 41, 2904-2916,
2007.

Kim, M.-H., Omar, A. H., Tackett, J. L., Vaughan, M. A., Winker, D. M., Trepte, C. R., Hu, Y., Liu, Z., Poole, L. R., Pitts, M. C., Kar, J., and Magill, B. E.: The CALIPSO Version 4 Automated Aerosol Classification and Lidar Ratio Selection Algorithm, Atmos. Meas. Tech. Discuss., https://doi.org/10.5194/amt-2018-166, in review, 2018.

Klett, J.: Stable analytical inversion solution for processing lidar returns, Appl. Optics, 20, 211–220, 1981.

Kumar, P., Sokolik, I. N., and Nenes, A.: Measurements of cloud condensation nuclei activity and droplet activation kinetics of fresh unprocessed regional dust samples and minerals, Atmos. Chem. Phys., 11, 3527-3541, doi:10.5194/acp-11-3527-2011, 2011a.

Kumar, P., Sokolik, I. N. and Nenes, A.: Measurements of cloud condensation nuclei activity and droplet activation kinetics of wet processed regional dust samples and minerals, Atmos. Chem. Phys., 11, 8661–8676, doi:10.5194/acp-11-8661-2011, 2011b.

Atmospheric
Chemistry
and Physics
Discussions

Levin, Z., Teller, A., Ganor, E., and Yin, Y.: On the interactions of mineral dust, sea-salt particles, and clouds: A measurement and modeling study from the Mediterranean Israeli Dust Experiment campaign, J. Geophys. Res., 110, D20202, doi:10.1029/2005JD005810, 2005.

Lohmann, U. and Feichter, J.: Global indirect aerosol effects: A review, Atmos. Chem. Phys., 5, 715-737, doi:10.5194/acp-5-715-2005, 2005.

Mamali, D., Marinou, E., Sciare, J., Pikridas, M., Kokkalis, P., Kottas, M., Binietoglou, I., Tsekeri, A., Keleshis, C., Engelmann, R., Baars, H., Ansmann, A., Amiridis, V., Russchenberg, H., and Biskos, G.: Vertical profiles of aerosol mass concentration derived by unmanned airborne in situ and remote sensing instruments during dust events, Atmos. Meas. Tech., 11, 2897-2910, https://doi.org/10.5194/amt-11-2897-2018, 2018.

Mamouri, R. E. and Ansmann, A.: Fine and coarse dust separation with polarization lidar, Atmos. Meas. Tech., 7, 3717-3735, https://doi.org/10.5194/amt-7-3717-2014, 2014.

Mamouri, R. E. and Ansmann, A.: Estimated desert-dust ice nuclei profiles from polarization lidar: Methodology and case studies, Atmos. Chem. Phys., 15, 3463-3477, doi:10.5194/acp-15-3463-2015, 2015.

Mamouri, R.-E. and Ansmann, A.: Potential of polarization lidar to provide profiles of CCN- and INP-relevant aerosol parameters, Atmos. Chem. Phys., 16, 5905-5931, doi:10.5194/acp-16-5905-2016, 2016.

Marinou, E., Amiridis, V., Binietoglou, I., Tsikerdekis, A., Solomos, S., Proestakis, E., Konsta, D., Papagiannopoulos, N., Tsekeri, A., Vlastou, G., Zanis, P., Balis, D., Wandinger, U., and Ansmann, A.: Three-dimensional evolution of Saharan dust transport towards Europe based on a 9-year EARLINET-optimized CALIPSO dataset, Atmos. Chem. Phys., 17, 5893-5919, doi:10.5194/acp-17-5893-2017, 2017.

Mason, R. H., Si, M., Chou, C., Irish, V. E., Dickie, R., Elizondo, P., Wong, R., Brintnell, M., Elsasser, M., Lassar, W. M., Pierce, K. M., Leaitch, W. R., MacDonald, A. M., Platt, A., Toom-Sauntry, D., Sarda-Estève, R., Schiller, C. L., Suski, K. J., Hill, T. C. J., Abbatt, J. P. D., Huffman, J. A., DeMott, P. J., and Bertram, A. K.: Size-resolved measurements of ice-nucleating particles at six locations in North America and one in Europe, Atmos. Chem. Phys., 16, 1637–1651, doi:10.5194/acp-16-1637-2016, 2016.

McFiggans, G., Artaxo, P., Baltensperger, U., Coe, H., Facchini, M. C., Feingold, G., Fuzzi, S., Gysel, M., Laaksonen, A., Lohmann, U., Mentel, T. F., Murphy, D. M., O'Dowd, C. D., Snid-er, J. R., and Weingartner, E.: The effect of physical and chemical aerosol properties on warm cloud droplet activation, Atmos. Chem. Phys., 6, 2593-2649, doi:10.5194/acp-6-2593-2006, 2006.

Morris, C.E., Conen, F., Alex Huffman, J., Phillips, V., Pöschl, U., Sands, D.C.: Bioprecipitation: A feedback cycle linking Earth history, ecosystem dynamics and land use through biological ice nucleators in the atmosphere, Global Change Biology, 20 (2), pp. 341-351, DOI:10.1111/gcb.12447, 2014.

Müller, D., A. Ansmann, I. Mattis, M. Tesche, U. Wandinger, D. Althausen, and G. Pisani: Aerosol-type-dependent lidar ratios observed with Raman lidar, J. Geophys. Res., 112, D16202, doi:10.1029/2006JD008292, 2007.

Murray, B. J., O'Sullivan, D., Atkinson, J. D., and Webb, M. E.: Ice nucleation by particles immersed in supercooled cloud droplets, Chem. Soc. Rev., 41, 6519–6554, doi:10.1039/c2cs35200a, 2012.

Nickovic, S., Kallos, G., Papadopoulos, A., and Kakaliagou, O.: A model for prediction of desert dust cycle in the atmosphere, J. Geophys. Res., 106, 18113–18129, 2001.

Nickovic, S., Cvetkovic, B., Madonna, F., Rosoldi, M., Pejanovic, G., Petkovic, S., and Nikolic, J.: Cloud ice caused by atmospheric mineral dust – Part 1: Parameterization of ice nuclei concentration in the NMME-DREAM model, Atmos. Chem. Phys., 16, 11367-11378, https://doi.org/10.5194/acp-16-11367-2016, 2016.

Niemand, M., Möhler, O., Vogel, B., Vogel, H., Hoose, C., Connolly, P., Klein, H., Bingemer, H., DeMott, P., Skrotzki, J., and Leisner, T.: parameterisation of immersion freezing on mineral dust particles: an application in a regional scale model, J. Atmos. Sci., 69, 3077–3092, 2012.

Nisantzi, A., Mamouri, R. E., Ansmann, A., Schuster, G. L., and Hadjimitsis, D. G.: Middle East versus Saharan dust extinction-to-backscatter ratios, Atmos. Chem. Phys., 15, 7071-7084, doi:10.5194/acp-15-7071-2015, 2015.

O'Sullivan, D., Murray, B.J., Malkin, T.L., Whale, T.F., Umo, N.S., Atkinson, J.D., Price, H.C., Baustian, K.J., Browse, J., Webb, M.E.: Ice nucleation by fertile soil dusts: relative importance of mineral and biogenic components. Atmospheric Chemistry and Physics, 14 (4), pp.
5   1853-1867, DOI:10.5194/acp-14-1853-2014, 2014.

O'Sullivan, D., Murray, B.J., Ross, J.F., Whale, T.F., Price, H.C., Atkinson, J.D., Umo, N.S., Webb, M.E.: The relevance of nanoscale biological fragments for ice nucleation in clouds, Scientific Reports, 5, art. no. A8082, DOI:10.1038/srep08082, 2015.

O'Sullivan, D., Murray, B.J., Ross, J.F., Webb, M.E.: The adsorption of fungal ice-nucleating proteins on mineral dusts: a terrestrial reservoir of atmospheric ice-nucleating particles, Atmospheric Chemistry and Physics, 16 (12), pp. 7879-7887, DOI:10.5194/acp-16-7879-2016,
10   2016.

Pérez, C., Nickovic, S., Baldasano, J., Sicard, M., Rocadenbosch, F., and Cachorro, V. E.: A long Saharan dust event over the western Mediterranean: Lidar, Sun photometer observations, and regional dust modeling, J. Geophys. Res., 111, D15214, doi:10.1029/2005JD006579, 2006.

Petters, M. D. and Kreidenweis, S. M.: A single parameter representation of hygroscopic growth and cloud condensation nucleus activity,
15   Atmos. Chem. Phys., 7, 1961-1971, doi:10.5194/acp-7-1961-2007, 2007.

Pruppacher, H. R. and Klett, J. D.: Microphysics of clouds and precipitation 2nd ed., Kluwer Academic Publishers, Boston, MA, 1997.

Rosenfeld, D., Andreae, M. O., Asmi, A., Chin, M., de Leeuw, G., Donovan, D. P., Kahn, R., Kinne, S., Kivekäs, N., Kulmala, M., Lau, W., Schmidt, K. S., Suni, T., Wagner, T., Wild, M. and Quaas, J.: Global observations of aerosol-cloud-precipitation-climate interactions, Rev. Geophys., 52, 750-808, doi:10.1002/2013RG000441, 2014.

20   Schnell R.C. and Vali G.: Biogenic ice nuclei: part I. Terrestrial and marine sources, J Atmos Sci., 33:1554–1564, 1976.

Schrod, J., Danielczok, A., Weber, D., Ebert, M., Thomson, E. S., and Bingemer, H. G.: Re-evaluating the Frankfurt isothermal static diffusion chamber for ice nucleation, Atmos. Meas. Tech., 9, 1313-1324, doi:10.5194/amt-9-1313-2016, 2016.

Schrod, J., Weber, D., Drücke, J., Keleshis, C., Pikridas, M., Ebert, M., Cvetković, B., Nickovic, S., Marinou, E., Baars, H., Ansmann, A., Vrekoussis, M., Mihalopoulos, N., Sciare, J., Curtius, J., and Bingemer, H. G.: Ice nucleating particles over the Eastern Mediterranean
25   measured by unmanned aircraft systems, Atmos. Chem. Phys., 17, 4817-4835, doi:10.5194/acp-17-4817-2017, 2017.

Seifert, P., Ansmann, A., Mattis, I., Wandinger, U., Tesche, M., Engelmann, R., Müller, D., Pérez, C., and Haustein, K.: Saharan dust and heterogeneous ice formation: Eleven years of cloud observations at a central European EARLINET site, J. Geophys. Res., 115, D20201, doi:10.1029/2009JD013222, 2010.

Seinfeld, J.H., Bretherton, C., Carslaw, K.S., Coe, H., DeMott, P.J., Dunlea, E.J., Feingold, G., Ghan, S., Guenther, A.B., Kahn, R., Krau-
30   cunas, I., Kreidenweis, S.M., Molina, M.J., Nenes, A., Penner, J.E., Prather, K.A., Ramanathan, V., Ramaswamy, V., Rasch, P.J., Ravishankara, A.R., Rosenfeld, D., Stephens, G. and Wood, R.: Improving our fundamental understanding of the role of aerosol-cloud interactions in the climate system, P. Natl. Acad. Sci., 113 (21), pp. 5781-5790. doi: 10.1073/pnas.1514043113, 2016.

Shimizu, A., N. Sugimoto, I. Matsui, K. Arao, I. Uno, T. Murayama, N. Kagawa, K. Aoki, A. Uchiyama, and A. Yamazaki: Continuous observations of Asian dust and other aerosols by polarization lidars in China and Japan during ACE-Asia, J. Geophys. Res., 109, D19S17,
35   doi: 10.1029/2002JD003253, 2004.

Steinke, I., Hoose, C., Möhler, O., Connolly, P., and Leisner, T.: A new temperature- and humidity-dependent surface site density approach for deposition ice nucleation, Atmos. Chem. Phys., 15, 3703–3717, doi:10.5194/acp-15-3703-2015, 2015.

Sullivan, S. C., Morales Betancourt, R., Barahona, D., and Nenes, A.: Understanding cirrus ice crystal number variability for different heterogeneous ice nucleation spectra, Atmos. Chem. Phys., 16, 2611-2629, https://doi.org/10.5194/acp-16-2611-2016, 2016.

Tackett, J. L., Winker, D. M., Getzewich, B. J., Vaughan, M. A., Young, S. A., and Kar, J.: CALIPSO lidar level 3 aerosol profile product: version 3 algorithm design, Atmos. Meas. Tech., 11, 4129-4152, https://doi.org/10.5194/amt-11-4129-2018, 2018.

5 Tao, W.-K., Chen, J.-P. , Li, Z, Wang, C. Zhang, C.: Impact of aerosols on convective clouds and precipitation, Rev. Geophys., 50, RG2001, doi:10.1029/2011RG000369, 2012.

Tesche, M., Ansmann, A., Müller, D., Althausen, D., Engelmann, R., Freudenthaler, V., and Groß, S.: Vertically resolved separation of dust and smoke over Cape Verde using multiwavelength Raman and polarization lidars during Saharan Mineral Dust Experiment 2008, J. Geophys. Res., 114, D13202, doi:10.1029/2009JD011862, 2009.

10 Tesche, M., Wandinger, U., Ansmann, A., Althausen, D., Müller, D., and Omar, A.H.: Ground-based validation of CALIPSO observations of dust and smoke in the Cape Verde region. J. Geophys. Res. Atmos., 118, 2889-2902, doi:10.1002/jgrd.50248, 2013.

Twohy, C. H., et al.: Saharan dust particles nucleate droplets in eastern Atlantic clouds, Geophys. Res. Lett., 36, L01807, doi:10.1029/2008GL035846, 2009.

Twohy, C. H., Anderson, B. E., Ferrare, R. A., Sauter, K. E., L'Ecuyer, T. S., van den Heever, S. C., Heymsfield, A. J., Ismail, S., and

15 Diskin, G. S.: Saharan dust, convective lofting, aerosol enhancement zones, and potential impacts on ice nucleation in the tropical upper troposphere, J. Geophys. Res. Atmos., 122, 8833-8851, doi:10.1002/2017JD026933, 2017.

Ullrich, R., Hoose, C., Möhler, O., Niemand, M., Wagner, R., Höhler, K., Hiranuma, H., Saathoff, H., and Leisner, T.: A new ice nucleation active site parameterization for desert dust and soot, J. Atmos. Sci., 74, doi:10.1175/JAS-D-16-0074.1, 2017.

Vali, G., DeMott, P. J., Möhler, O., and Whale, T. F.: Technical Note: A proposal for ice nucleation terminology, Atmos. Chem. Phys., 15,

20 10263-10270, doi:10.5194/acp-15-10263-2015, 2015.

Vergara-Temprado, J., Murray, B.J., Wilson, T.W., O'Sullivan, D., Browse, J., Pringle, K.J., Ardon-Dryer, K., Bertram, A.K., Burrows, S.M., Ceburnis, D., Demott, P.J., Mason, R.H., O'Dowd, C.D., Rinaldi, M., Carslaw, K.S.: Contribution of feldspar and marine organic aerosols to global ice-nucleating particle concentrations, Atmospheric Chemistry and Physics, 17 (5), 3637–3658, DOI:10.5194/acp-17-3637-2017, 2017.

25 Weinzierl, B., Petzold, A., Esselborn, M., Wirth, M., Rasp, K., Kandler, K., Schütz, L., Koepke, P., and Fiebig, M.: Airborne measurements of dust layer properties, particle size distribution and mixing state of Saharan dust during SAMUM 2006, Tellus B, 61, 96-117, doi:10.1111/j.1600-0889.2008.00392.x, 2009.

Westbrook, C. D. and Illingworth A. J.: Evidence that ice forms primarily in supercooled liquid clouds at temperatures $> -27\,^{\circ}$C, Geophys. Res. Lett., 38, L14808, doi:10.1029/2011GL048021, 2011.

30 Wilson, T.W., Ladino, L.A., Alpert, P.A., Breckels, M.N., Brooks, I.M., Browse, J., Burrows, S.M., Carslaw, K.S., Huffman, J.A., Judd, C., Kilthau, W.P., Mason, R.H., McFiggans, G., Miller, L.A., Najera, J.J., Polishchuk, E., Rae, S., Schiller, C.L., Si, M., Temprado, J.V., Whale, T.F., Wong, J.P.S., Wurl, O., Yakobi-Hancock, J.D., Abbatt, J.P.D., Aller, J.Y., Bertram, A.K., Knopf, D.A., Murray, B.J.: A marine biogenic source of atmospheric ice-nucleating particles, Nature, 525 (7568), pp. 234-238, DOI:10.1038/nature14986, 2015.

Winker, D. M., Vaughan, M. A., Omar, A., Hu, Y., Powell, K. A., Liu, Z., Hunt, W. H., and Young, S. A.: Overview of the CALIPSO Mission

35 and CALIOP Data Processing Algorithms, J. Atmos. Oceanic Tech., 26, 2310-2323, doi:10.1175/2009JTECHA1281.1, 2009.

Atmospheric
Chemistry
and Physics
Discussions
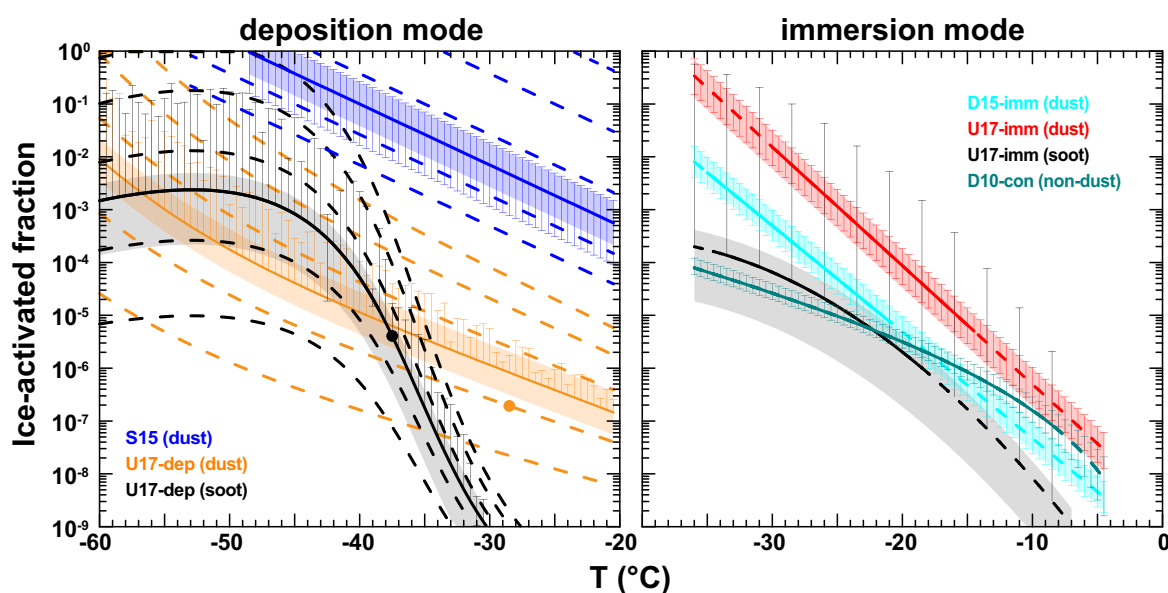
Figure 1. Fraction of ice activated particles for the deposition nucleation (left) and immersion freezing (right) parameterisations used in this study. The particle concentrations used are derived assuming an extinction coefficient of $50 \, \mathrm{Mm}^{-1}$ for each of the different aerosol types (dust, continental, soot). The shaded areas take into account a range of the extinction coefficient from $10 \, \mathrm{Mm}^{-1}$ (lower limit) to $200 \, \mathrm{Mm}^{-1}$ (upper limit). The error bars mark the error of the respective parameterisations from error propagation using the uncertainties provided in Table 2. Negative error bars that exceed the scale are not shown. In the deposition mode (left) panel, the bold lines correspond to ice supersaturation of 1.15 and the dashed lines to ice supersaturation of 1.05, 1.1, 1.2, 1.3 and 1.4. The black and orange dots indicate the maximum temperatures for which the parameterizations have been developed.
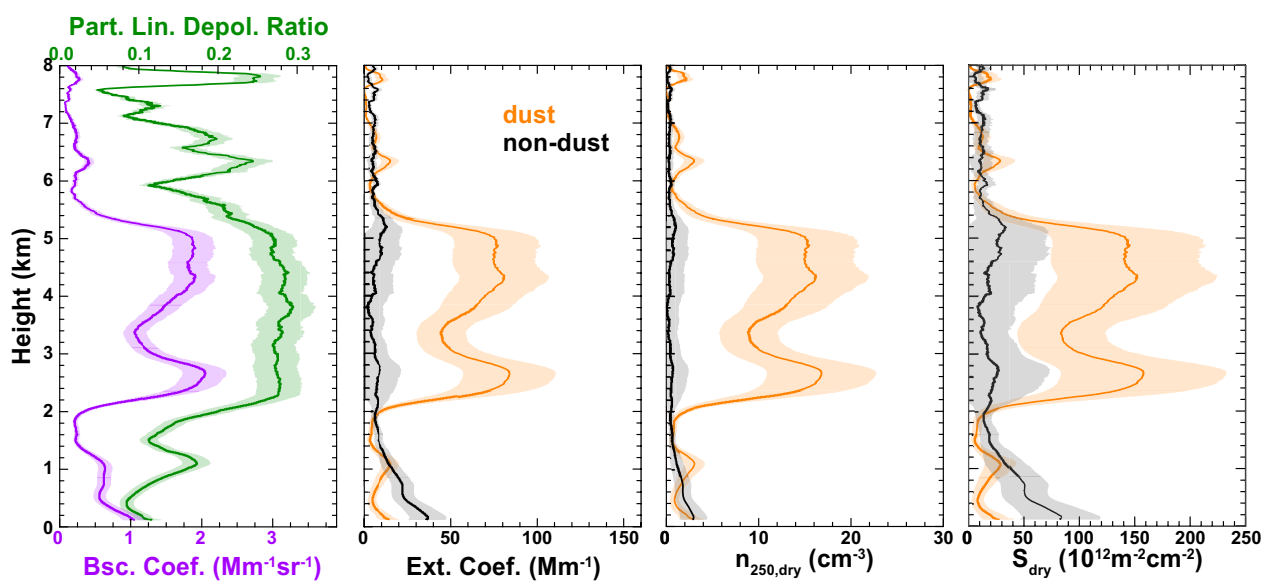
Figure 2. PollyXT profiles of the total particle backscatter coefficient (purple) and particle linear depolarisation ratio (green) measured between 1 and 2 UTC on 21 April 2016. The extinction coefficient as well as the number and surface concentration of particles with a dry radius larger than 250 nm related to mineral dust (orange) and non-dust aerosol (black) was obtained following the methodology described in Section 3.2.

Atmospheric
Chemistry
and Physics
Discussions
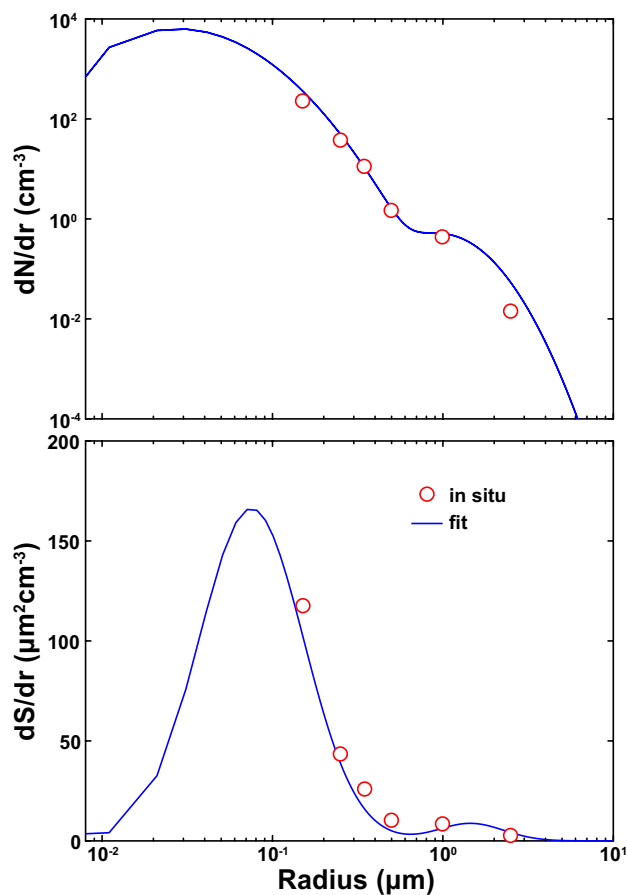
Figure 3. (a) The number size distribution used for the estimation of the corrected $n_{250,dry}$ (number concentration of particles with radius larger than 250 nm) and (b) the corresponding surface size distribution used for the estimation of the corrected S_{dry} (surface concentration of all particles). In-situ measurements are denoted by red circles while the blue lines give the bimodal log-normal fit on the measurements. The example refers to the UAV-OPC data acquired at 1.2 km at 1045 UTC on 5 April 2016 (see Figure 6).

Atmospheric
Chemistry
and Physics
Discussions
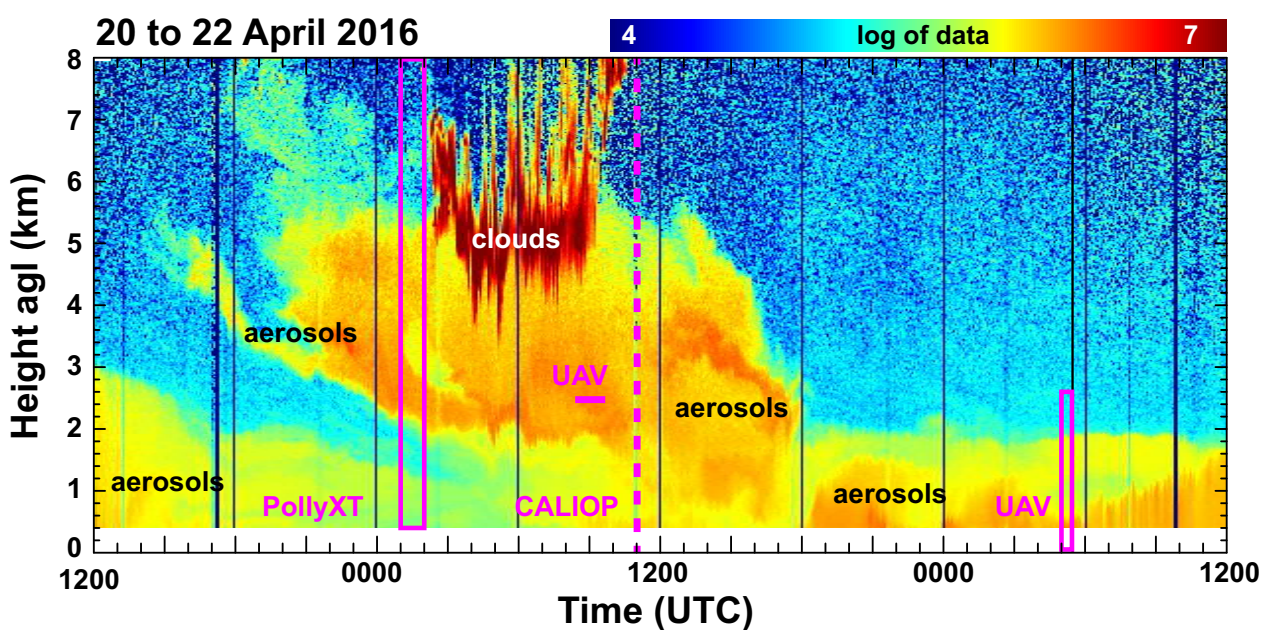
Figure 4. Time-height display of the 1064-nm range-corrected signal measured with PollyXT between 12 UTC on 20 April 2016 and 12 UTC on 22 April 2016. The magenta markers refer to the analysed period of PollyXT (left box, 1 - 2 UTC on 21 April 2016), CALIOP (dashed line, 11:01 UTC on 21 April 2016) and UAV (horizontal bar, INP sampling between 8:30 and 9:40 UTC on 21 April 2016 and right box, OPC measurements between 5:00 and 5:30 UTC on 22 April 2016) that are being referred to in this study. Vertical black lines in the lidar plot mark missing data.

Atmospheric
Chemistry
and Physics
Discussions
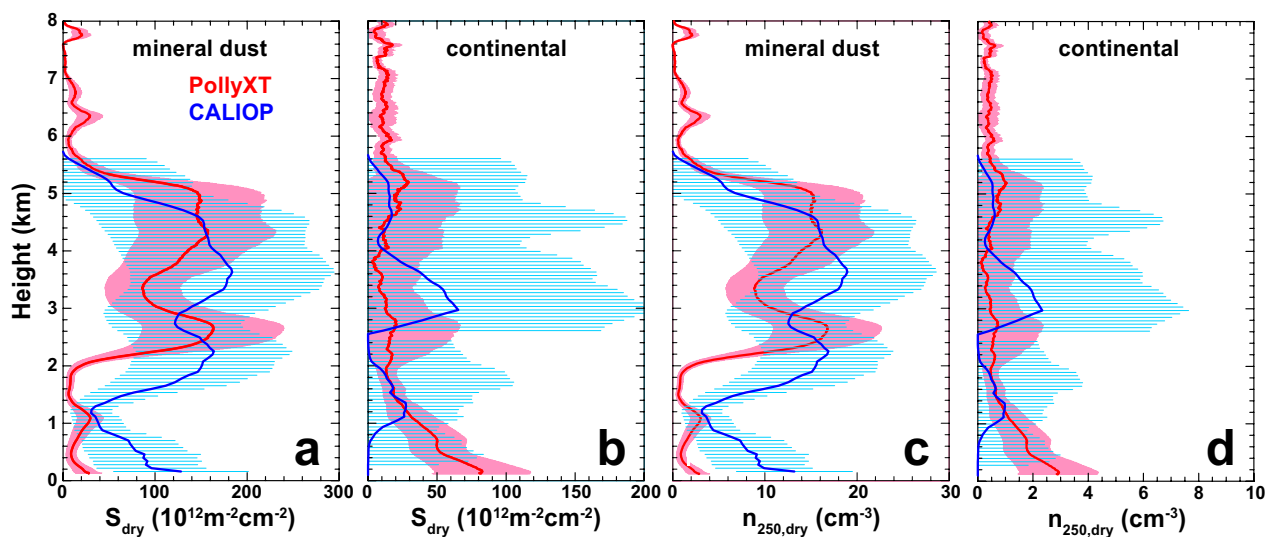
Figure 5. Profiles of the surface (a, b) and number concentrations (c, d) of mineral dust (a, c) and continental particles (b, d) with a dry radius larger than 250 nm derived from measurements with PollyXT between 1 and 2 UTC on 21 April 2016 (red) and retrieved from averaging 160 km of CALIOP measurements centred around an overpass at a distance of 5 km from Nicosia at 11:01 UTC on 21 April 2016 (blue).
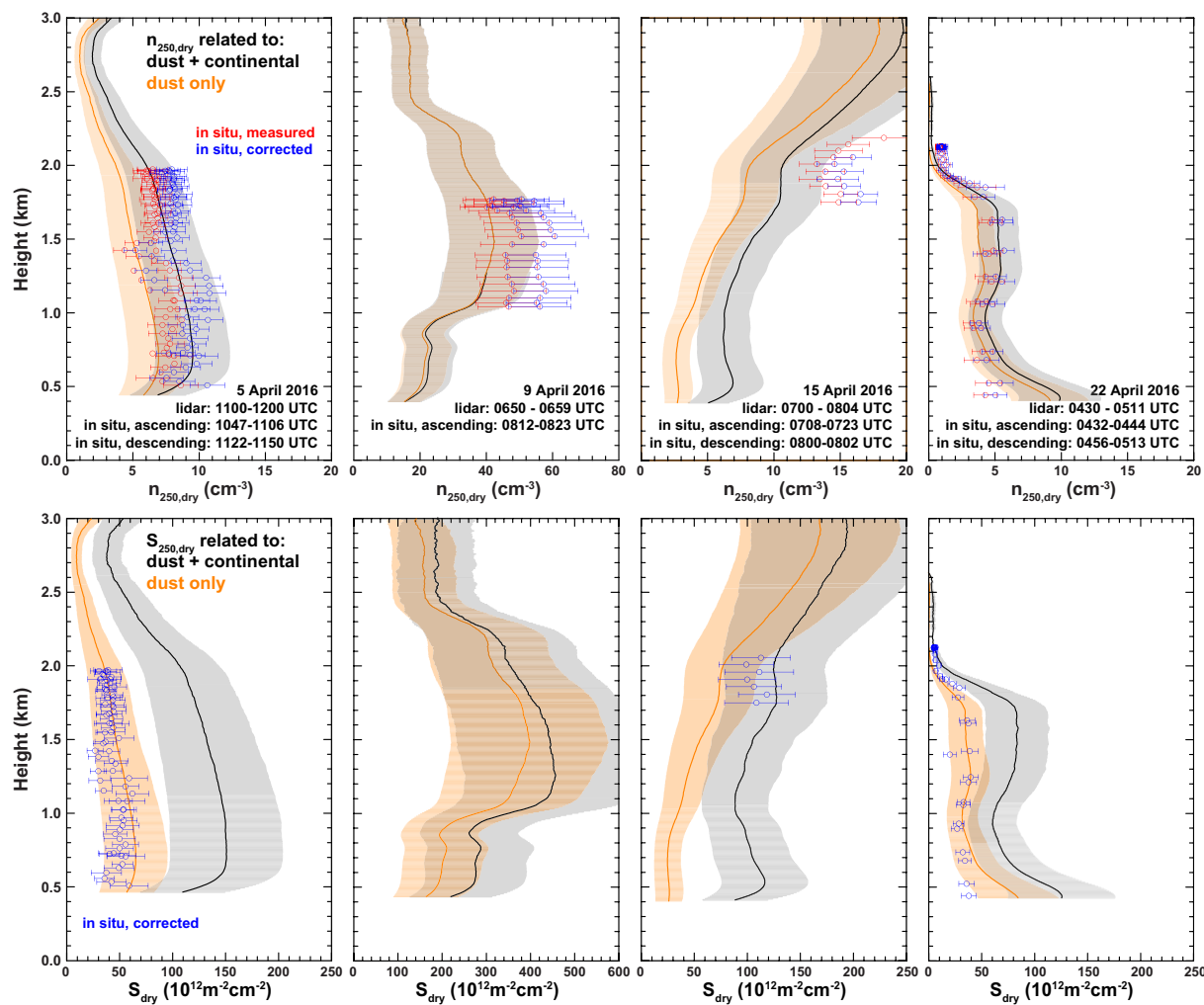
Figure 6. Profiles of $n_{250,dry}$ (upper panel) and S_{dry} (lower panel) obtained from PollyXT and in-situ measurements (UAV uncorrected data in red, UAV corrected data in blue) on 5, 9, 15 and 22 April 2016. The lidar-derived profiles refer to dust only concentrations (orange), as well as the combination of dust and continental pollution concentrations (black).
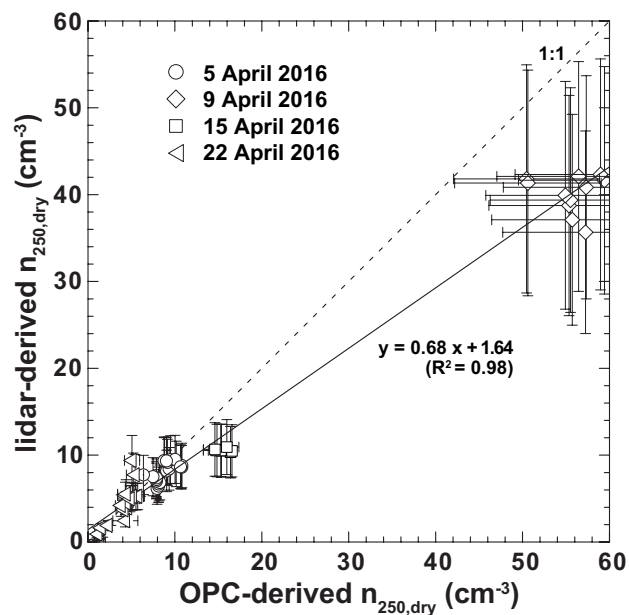
Figure 7. Correlation plot of $n_{250,dry}$ obtained from drone-based OPC measurements and inferred from lidar observations (values for a mixture of mineral dust and continental pollution, black in in Figure 6) during coordinated activities on 5, 9, 15 and 22 April 2016. The solid line marks the linear regression with the corresponding function and squared correlation coefficient given in the plot. The 1:1 line is given as dashed line.

Atmospheric
Chemistry
and Physics
Discussions
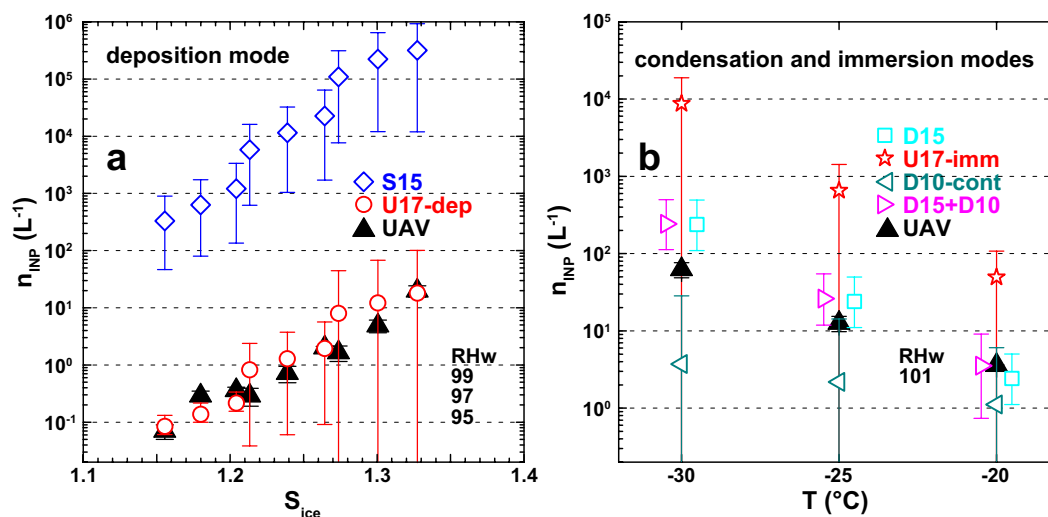
Figure 8. INP concentrations (n_{INP}) estimated from the lidar measurements on 21 April 2016 presented in Figure 6 (coloured symbols) and the UAV-FRIDGE measurements (black triangles) for (a) deposition freezing (as a function of saturation over ice) and (b) condensation and immersion freezing (as a function of temperature). Data in (a) are obtained for values of relative humidity over water of 95%, 97%, and 99%, leading to three values of S_{ice} for each analysed temperature. A relative humidity over water of 101% is used to obtain the values presented in (b).
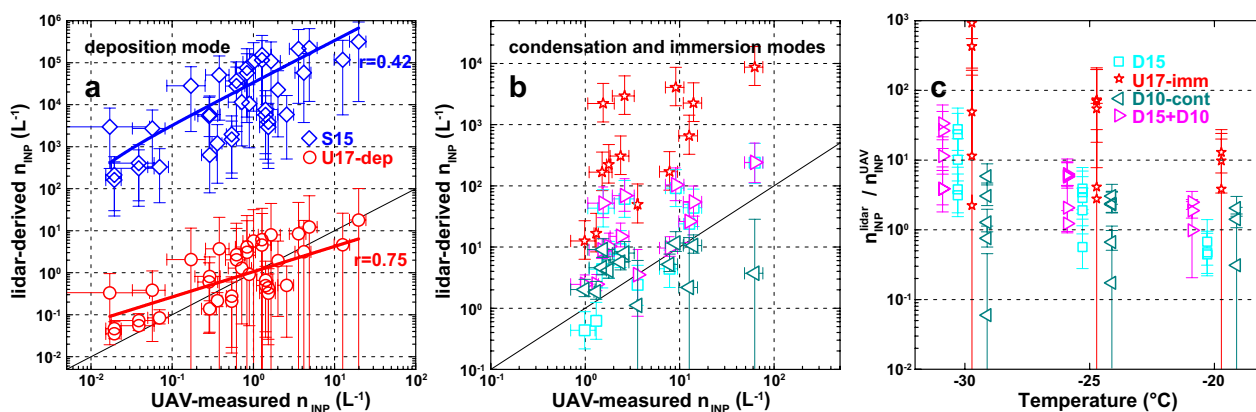
Figure 9. Comparison of INP concentrations derived from the lidar observations and UAV-FRIDGE measurements for (a) deposition freezing and (b) condensation and immersion freezing as well as (c) in form of the ration of lidar-derived and UAV-measured values for different temperature intervals for the observations on 5, 15 and 21 April 2016. Colours and symbols refer to the used parameterization. Lines in (a) and (b) mark the 1:1 line. Numbers in (a) give Pearson's r of the linear fits.

Atmospheric
Chemistry
and Physics
Discussions
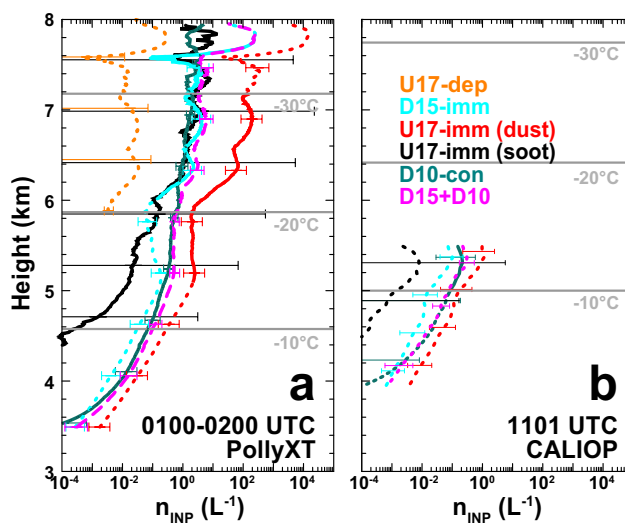
Figure 10. INP concentration profiles estimated from the measurements with (a) Polly between 0100 and 0200 UTC on 21 April 2016 and (b) CALIOP at 1101 UTC on 21 April 2016. Temperature levels have been extracted from a nearby WRF profile. Colours refer to different INP parameterisations. Solid lines mark the temperature range for which the corresponding parameterisation has been developed. Dashed lines refer to the extrapolated temperature range (see Table 1).

Atmospheric
Chemistry
and Physics
Discussions

Table 1. Overview of INP parameterizations used in this study together with the freezing mode and the temperature range for which they have been developed. The parameterizations of D15 and U17-imm have been extrapolated to the temperature range from $-36\,^\circ$C to $-1\,^\circ$C. In the equations, $n_{250,\mathrm{dry}}$ is in cm^{-3}, n_{INP} in L^{-1}, $T(z)$ in K and P in hPa. p_0 and T_0 hold for standard pressure and temperature.

Parameterization name	Reference	Mode	T ($^\circ$C)	Parameterization, $n_{\mathrm{INP}} =$	Eq.
Dust:					
U17-imm	Ullrich et al. (2017)	immersion	-30 to -14	$S_{\mathrm{d,dry}}\,n_{\mathrm{s}}(T)$	(1)
				with $n_{\mathrm{s}}(T) = \exp\left[150.577 - 0.517(T - 273.16)\right]$	
D15	DeMott et al. (2015)	immersion	-35 to -21	$[n_{250,\mathrm{d,dry}}(p_0, T_0)^{[a_1(273.16-T)+b_1]}\exp\left[c_1(273.16 - T) + d_1\right]](T_0 p)/(T p_0)$	(2)
		condensation		with $a_1 = 0.0$, $b_1 = 1.25$, $c_1 = 0.46$, $d_1 = -11.6$	
U17-dep	Ullrich et al. (2017)	deposition	-67 to -33	$S_{\mathrm{d,dry}}\,n_{\mathrm{s}}(T, S_{\mathrm{ice}})$	(3)
				with $n_{\mathrm{s}}(T, S_{\mathrm{ice}}) = \exp\left[a_2(S_{\mathrm{ice}} - 1)^{\frac{1}{4}}\cos\left[b_2(T - \gamma_2)\right]^2 \operatorname{arccot}\left[\kappa_2(T - \lambda_2)\right]/\pi\right]$	
				and $a_2 = 285.692$, $b_2 = 0.017$, $\gamma_2 = 256.692$, $\kappa_2 = 0.080$, $\lambda_2 = 200.745$	
S15	Steinke et al. (2015)	deposition	-53 to -20	$S_{\mathrm{d,dry}}\,n_{\mathrm{s}}(T)$	(4)
				with $n_{\mathrm{s}}(T) = 1.88 \times 10^5 \exp\left(0.2659\,\chi(T, S_{\mathrm{ice}})\right)$	
				and $\chi(T, S_{\mathrm{ice}}) = -(T - 273.2) + (S_{\mathrm{ice}} - 1) \times 100$	
Soot:					
U17-imm	Ullrich et al. (2017)	immersion	-34 to -18	$S_{\mathrm{c,dry}}\,n_{\mathrm{s}}(T)$	(5)
				with $n_{\mathrm{s}}(T) = 7.463\exp\left[-0.0101(T - 273.15)^2 - 0.8525(T - 273.15) + 0.7667\right]$	
U17-dep	Ullrich et al. (2017)	deposition	-78 to -38	$S_{\mathrm{c,dry}}\,n_{\mathrm{s}}(T, S_{\mathrm{ice}})$	(6)
				with $n_{\mathrm{s}}(T, S_{\mathrm{ice}}) = \exp\left[a_3(S_{\mathrm{ice}} - 1)^{\frac{1}{4}}\cos\left[b_3(T - \gamma_3)\right]^2 \operatorname{arccot}\left[\kappa_3(T - \lambda_3)\right]/\pi\right]$	
				and $a_3 = 46.021$, $b_3 = 0.011$, $\gamma_3 = 248.560$, $\kappa_3 = 0.148$, $\lambda_3 = 237.570$	
Non-dust:					
D10	DeMott et al. (2010)	immersion	-35 to -9	$[a_4(273.16 - T)^{b_4}n_{250,\mathrm{c,dry}}(p_0, T_0)^{[c_4(273.16-T)+d_4]}](T_0 p)/(T p_0)$	(7)
		condensation		with $a_4 = 0.0000594$, $b_4 = 3.33$, $c_4 = 0.0265$, $d_4 = 0.0033$	

Atmospheric
Chemistry
and Physics
Discussions

Open Access

Table 2. Values and typical uncertainties used for the estimation of f_i, α_d, α_c, $S_{d,dry}$, $S_{c,dry}$, $n_{250,d,dry}$, $n_{250,c,dry}$ and n_{INP}.

Parameter	Value	Reference
β_p	$0.15\,\beta_p$	
α_p	$0.2\,\alpha_p$	(only for f_i estimations)
δ_p	$0.15\,\delta_p$	
δ_d	0.31 ± 0.04	Freudenthaler et al. (2009); Ansmann et al. (2011)
δ_{nd}	0.05 ± 0.03	Müller et al. (2007); Groß et al. (2013); Baars et al. (2016); Haarig et al. (2017)
S_d	$45 \pm 11\,\mathrm{sr}$	Nisantzi et al. (2015)
S_c	$50 \pm 25\,\mathrm{sr}$	Baars et al. (2016)
$c_{250,d}$	$0.20 \pm 0.03\,\mathrm{Mm\,cm^{-3}}$	Mamouri and Ansmann (2016) (Cape Verde, Barbados, Germany)
$c_{s,d}$	$(1.94 \pm 0.68)\,10^{-12}\,\mathrm{Mm\,m^2\,cm^{-3}}$	Mamouri and Ansmann (2016) (Cape Verde, Barbados)
$c_{290,c}$	$0.10 \pm 0.04\,\mathrm{Mm\,cm^{-3}}$	Mamouri and Ansmann (2016) (Germany)
$c_{s,c}$	$(2.80 \pm 0.89)\,10^{-12}\,\mathrm{Mm\,m^2\,cm^{-3}}$	Mamouri and Ansmann (2016) (Germany)
δ_T	$2\,\mathrm{K}$	DeMott et al. (2017)
S_{ice}	$1.15 \pm 0.05\,S_{ice}$	DeMott et al. (2017)

Table 3. Overview of the AERONET-based parameterizations used in this study for the conversion of the measured optical aerosol properties (α_d, α_c) into the microphysical properties ($n_{250,d,dry}$, $S_{d,dry}$, $n_{250,c,dry}$ and $S_{c,dry}$). The parameterizations were introduced in Mamouri and Ansmann (2016). In the equations, α is in $\mathrm{Mm^{-1}}$, c_{250} in $\mathrm{Mm\,cm^{-3}}$, c_s in $\mathrm{Mm\,m^2\,cm^{-3}}$, $n_{250,dry}$ in $\mathrm{cm^{-3}}$ and S_{dry} in $\mathrm{m^2 cm^{-3}}$. For the values of the conversion parameters ($c_{250,d}$, $c_{s,d}$, $c_{250,c}$ and $c_{s,c}$) see Table 2.

Parameterization	Eq.
Dust:	
$n_{250,d,dry} = c_{250,d}, \times \alpha_d$	(8)
$S_{d,dry} = c_{s,d} \times \alpha_d$	(9)
Non-dust, continental:	
$n_{250,c,dry} = c_{250,c} \times \alpha_c$	(10)
$S_{c,dry} = c_{s,c} \times \alpha_c$	(11)

Atmospheric
Chemistry
and Physics
Discussions
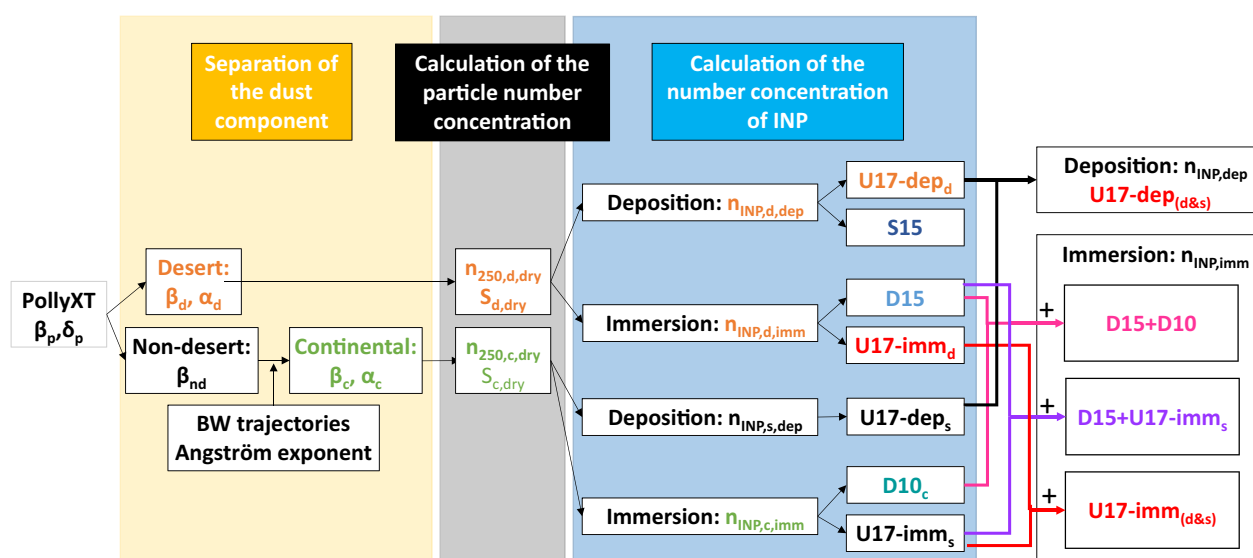
Figure A1. Overview of the data analysis scheme followed for the PollyXT measurements in this work. In the first step, we separate desert and non-desert backscatter coefficients (β_d and β_{nd}) by means of the particle linear depolarization ratio (δ_p). The backscatter coefficients for the non-desert aerosol is estimated to be continental aerosol mixtures β_c by means of, e.g., backward (BW) trajectory analysis and Ångström exponent information. The two backscatter coefficients are then converted to aerosol-type-dependent particle extinction coefficients (α_i). In the next step, the extinction coefficients are converted to aerosol-type-dependent profiles of particle number concentrations ($n_{250,i,dry}$) and particle surface area concentration ($S_{i,dry}$). In the next step, ice-nucleating particle number concentrations ($n_{INP,i}$) are estimated by applying INP parameterisations from the literature indicated by D10, D15, S15, U17 for DeMott et al. (2010), DeMott et al. (2015), Steinke et al. (2015) and Ullrich et al. (2017), respectively. Finally, the INP concentrations estimated for the different aerosol types are summed in order to estimate the total n_{INP}.

Atmospheric
Chemistry
and Physics
Discussions
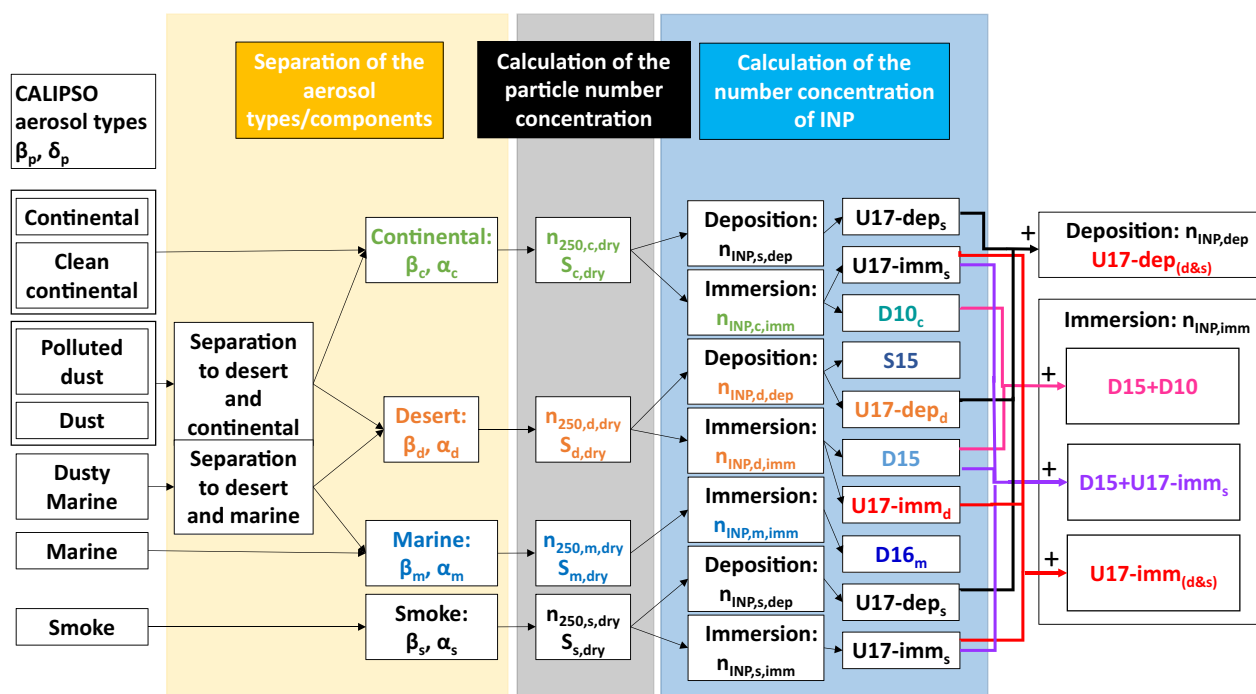
Figure A2. Overview of the data analysis scheme applied to CALIPSO measurements. In the CALIPSO case considered in this work only dust and polluted dust aerosol types have been observed. For that reason, only these combinations are considered here.